Imperial College London

Department of Mechanical Engineering

ME4 Individual Project

'Topology Optimisation of Lattice Structure Additive Manufactured Knee Implants'

Final Report

Author:	Asad Raja
Supervisor:	Jonathan Jeffers
Date:	03/06/21
Word Count:	11992 / 12000

ABSTRACT

The Mechanical Engineering Department's Biomechanics Research Group are in the process of developing an additive manufactured, lattice structure knee implant. A common drawback of standard modern knee implants is that their modulus, typically around 110 GPa, is far greater than the surrounding bone tissue which impedes effective bone regeneration. The modulus of the Biomechanics Group's implant will be much lower, to match the surrounding bone and allow for better bone regeneration.

The aim of this project was to optimise the topology of the tibial tray of this knee implant by adjusting the volume fraction throughout the lattice structure, such that its fatigue strength is more in line with the standard set by the ISO14879 test method. A compromise was to be reached in doing so between ensuring a sufficient strength for fatigue performance and maintaining a modulus that is sufficiently comparable with the surrounding bone to gain the benefit of effective bone regeneration.

Conducting a non-penalising stiffness-maximising topology optimisation with constraints upon the average regional modulus-matching improved the structure's yield performance when exposed to the ISO test-specified 900 N load compared to a fully modulus-matched structure. With a 14.3% average deviation from the ideal bone regeneration modulus targets, the predicted percentage of element failures in a mesh of the tibial tray was reduced by approximately 16.9%. Integrating a stress solver into the simulation allowed a looped process to be developed, whereby volume fractions were adjusted to prevent failure according to an initial stress distribution, before finding the updated stress distribution caused by this adjustment and repeating. Significant sensitivity to initial conditions and iteration number in this process offered a wide range of potential design solutions. With an initial condition of a fully modulus-matched structure, a single iteration of the looped process resulted in a design that reduced percentage predicted element failures by approximately 44.9%, with a 12% average deviation from the modulus targets.

A non-penalising stress-constrained topology optimisation approach would have a powerful potential application to this problem. Developing such a simulation would be highly novel and complex. Groundwork was set for this approach by deriving an analytical solution for clustered stress sensitivity values, although further consideration would be needed for successful validation.

CONTENTS

ACKNOWLEDGEMENTS

1. INTRODUCTION

Knee implant design is an area of increased focus in engineering, with medical advances and trends in the age, gender and BMI of populations leading to increased reliance upon them. Knee implants are a relevant option for surgeons undertaking joint preservation or early intervention partial joint replacement surgeries, but the most significant use-case is the total knee arthroplasty [1]. Based upon 2010 total knee arthroplasty incident rates, with projected BMI and age trends accounted for, the estimated number of total knee arthroplasties in the UK increases by 25%, from 94,783 in 2020 to 118,666 in 2035 [2]. Figure 1 indicates the effects of trends in BMI and age distribution on incident number trends.
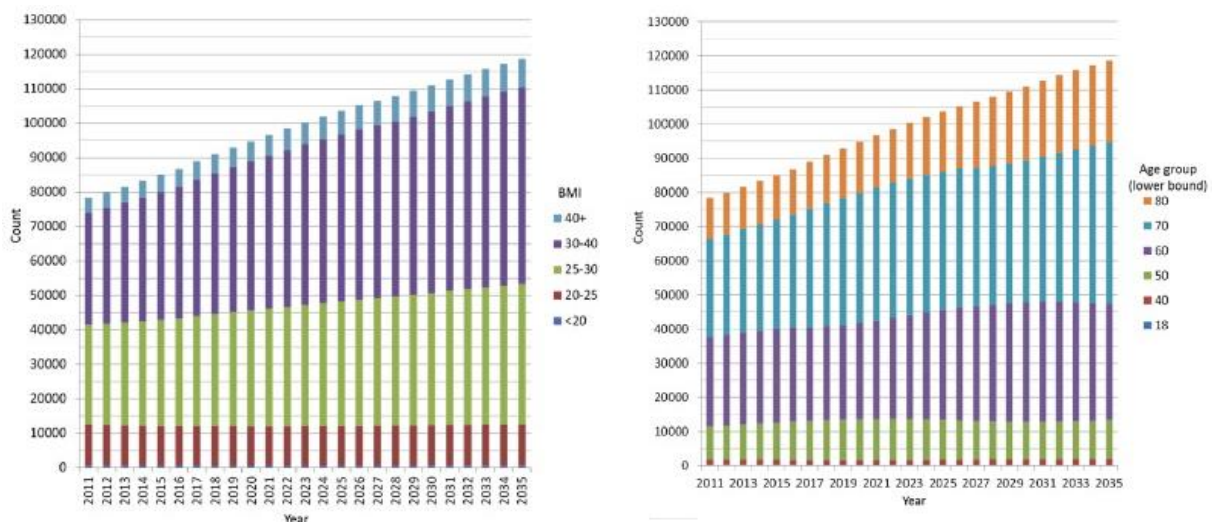
FIGURE 1 – TOTAL KNEE ARTHROPLASTY INCIDENT TRENDS [2]

The total knee arthroplasty procedure is a common treatment in cases of injury or arthritis where non-surgical options have been exhausted. The procedure involves a resurfacing of the ends of the tibia and femur with metal implant components before a spacer is inserted between the two bones to create a smooth gliding surface for movement at the joint [3]. The tibia resurfacing component, shown in Figure 2, is known as the tibial tray and is the focus of this project. Although total knee arthroplasty is among the safest procedures in all of medicine, its increased frequency has led to a growing number of complications and revision procedures [4].
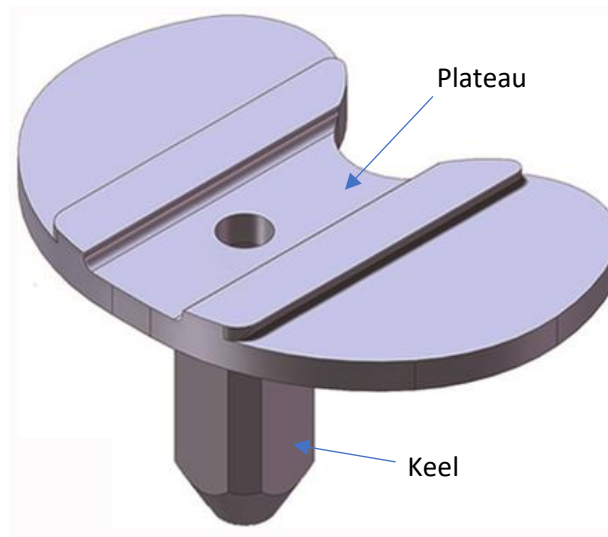
The Biomechanics Research Group at Imperial College London are part of the Medical Engineering Group within the Applied Mechanics Divisions of the Mechanical Engineering Department. The group specialises in synthesising novel engineering solutions to orthopaedic problems, and utilising cutting-edge technology to develop orthopaedic devices. A recent area of work in the Biomechanics Group has been the development of additive manufactured knee implant components from a titanium alloy (Ti6Al4V) lattice structure material. The use of a lattice structure as opposed to solid titanium typically employed in the tibial tray is hoped to improve anisotropic properties and better match mechanical properties in the tibia, to maintain natural load transfer and thus improve bone remodelling, thereby reducing the likelihood of complication and the need for revision procedures. Specifically, this can be achieved by the matching of modulus values between the implant and bone. The work is being conducted by PhD student Maxwell Munford, who has acted as the co-supervisor of this project.

Additive manufacture opens the window for structures to have controlled, favourable anisotropy by means of an optimised lattice architecture, such that strengths and moduli along axes are tailored to directional needs and adequate mechanical properties are provided in all directions. This demands an ability to predict the anisotropic properties of the lattice structure. A method of doing so has been developed by the Biomechanics Group, relating mechanical test data for material properties in principal component directions to structural density and fabric with a power law fitting [6]. For favourable bone remodelling characteristics, with matched bone and implant mechanical properties, a map of bone apparent modulus in the axial and transverse directions through the tibia is required. Such a mapping has been achieved by the Biomechanics Group, with

a resulting understanding of material property locational dependence and a relationship established with bone density values as obtained from conventional clinal CT scans [7].

1.1. AIMS AND OBJECTIVES

The research thus far has resulted in the development of a lattice structure tibial tray, with local volume fractions through the structure selected to match the surrounding bone. It has been shown that the load transfer to the tibia resulting from this design is very close to the original un-implanted case, which improves bone remodelling behaviour by means of the bone's natural homeostasis. **The aim of this project was to adapt the design of the lattice structure knee implant to improve fatigue strength in accordance with the ISO certification, whilst maintaining the favourable bone remodelling properties**. The certification defines the minimum endurance strength required of the tibial tray according to whether the ISO14879 load cycle testing is passed.

The objectives to be met to achieve this aim are detailed.

1. Conduct a literature review to understand the following:
   - Bone remodelling theory.
   - The requirements of the ISO14879 test method.
   - Fatigue behaviour of lattice structure, additive manufactured materials.
   - The concept of topology optimisation.

2. Conduct a standard SIMP stiffness topology optimisation.

3. Implement a non-binary stiffness topology optimisation approach.

4. Implement a stress solver to assess the optimisations according to stress limits and develop hybrid stress-satisfying designs.

5. Develop a non-binary stress topology optimisation.

6. Define and compare the strength and remodelling potential of each considered design.

7. Conduct ISO14879 or other lab testing on additive manufactured specimens to validate designs.

Literature on non-binary topology optimisations was sparse and therefore a novel approach would have to be taken to developing these. The area of stress topology optimisation is also complex and under-researched, with stiffness topology optimisation methods being far more established. It was therefore understood that developing a non-binary stress topology optimisation method would be

especially challenging, and this was therefore identified as a secondary area of investigation in attempting to achieve the project aim. Developing a non-penalising stiffness topology optimisation and stress satisfying and hybrid stress satisfying approaches would take precedent. At the time of writing this report, designs have been additive manufactured, but testing has been left as a next step to this work due to time constraints.

2. BACKGROUND AND LITERATURE REVIEW

2.1.   KNEE IMPLANTS FOR IMPROVED BONE REMODELLING

The tibial tray of a knee implant is the component that re-surfaces the tibia in order to support and secure the articulating surface component, as shown in Figure 3. The tibial tray is subject to significant loads during activities of daily living, varying, as a percentage of body weight, from 107% BW at two-legged standing to 346% BW during stair descending [8]. Though solid titanium alloy implant materials (Ti6Al4V) typically used at present can withstand these loads, they have modulus values in the region of 110 GPa, whilst the tibia has modulus value of 0.3-5 GPa. The mismatch in implant modulus compared with that of the surrounding bone is associated with a stress shielding effect [9]. As proposed by Wolff's Law, repetitive loading of bone causes an adaptive response which enables the bone to better withstand the loads [10]. This confirms Frost's mechanostat theory, which presents the concept of bone metabolic monitoring in relation to its mechanical usage to stimulate modelling and remodelling behaviour as needed [11]. It is also understood that below a certain strain or loading threshold, bone material is resorbed [12]. It has therefore been observed that when stress shielding prevents stresses from being translated from the implant to the tibia, inferior bone remodelling and bone weakening results, eventually resulting in aseptic loosening of the implant. This is a major source of complication for total knee arthroplasty [13].

FIGURE 3 – KNEE IMPLANT COMPONENTS [14]

To overcome this limitation, lattice structure titanium implants such as that being developed by the Biomechanics Group, have recently become a source of interest [15]. Lattice structures hold the potential advantage of efficient mass distribution and optimised material properties such as modulus, compressive weight-to-strength ratio, or natural frequency. They also allow mechanical anisotropy to be specially designed for the application [6]. Recent developments of additive manufacturing methods have allowed these advantages of lattices to be achieved through finer control of their structure. The most common additive manufacturing process is selective laser melting, which fabricates the structure by fusing fine metal powders. It is hoped that the regional modulus of the additive manufactured tibial tray can be matched to the tibial modulus as it varies through the bone location [7], by varying the porosity appropriately through the structure. This has the potential to better-translate loading from the implant to the surrounding bone. By preventing stress shielding and encouraging tissue ingrowth, the implant may be stabilised, thus reducing the possibility of complication, improving its longevity [15]. The pore interconnection offered by a lattice structure would also be advantageous for cell migration and in vivo blood vessel formation. However, the material properties will be worsened with porosity. It is therefore important to determine whether a compromise can be reached between the improvement in bone regeneration offered by the lattice implant and the achievement of minimum strength requirements, defined by the ISO 14879 test.

2.2. ISO TEST

The ISO 14879 test is a tibial tray endurance test method. Placing the test specimen in a rig with one end fixed, the other extends as a cantilever with a cyclic force applied to it through a spacer as shown in Figure 4. The test method establishes an endurance requirement of 5 specimens passing 10 million cycles of a 900 N load. The position of the loading point is to correspond with the centre of pressure when the femoral component, articulating surface and tibial tray are assembled at 0 flexion, and the frequency of loading is to be no greater than 10 Hz [16]. For a left-hand side tibial tray, this loading location is near the centre of the right-side plateau region, and vice versa for a right-hand side component.
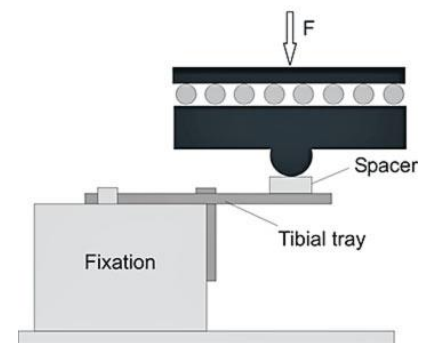

FIGURE 4 – ISO 14879 SCHEMATIC [16]

2.3. FATIGUE BEHAVIOUR OF ADDITIVE MANUFACTURED LATTICE STRUCTURES

Lattice structures or cellular solids are solids made up of a network of edges or faces constructing distinct cells. Within open cell cellular material – the lattice structure type employed in this project – edges or struts which meet at vertices are the main constructing element as shown in Figure 5.
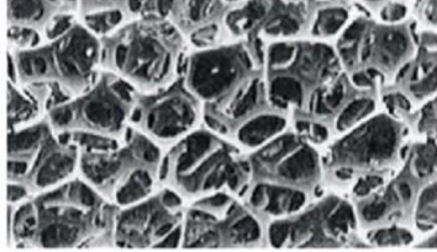
FIGURE 5 - OPEN CELL CELLULAR MATERIAL [17]

The struts are susceptible to three potential failure mechanism – yielding, buckling or fracture – with failure occurring by means of that with the lowest stress threshold [18]. The lattice structures can be further categorised as either stretch dominated, whereby the struts experience axial stress, or bending dominated, where the macro stress induces bending moments in the struts. The stress-strain behaviour for the two modes is distinct, as shown in Figure 6, resulting in different failure mechanisms. The bending dominated mode, which is less stiff than the stretch dominated, may result in crack initiation at the outer fibres of struts where the tension stresses are greatest, which leads to crack propagation and eventual strut fracture [19]. The Maxwell number, as described in Equation 1, is a possible way of classifying the dominated mode, where s is the number of interacting struts and n is the number of nodes. $M < 0$ suggests a bending dominant structure whereas $M \geq 0$ suggests stretch dominant, however this definition is limited since it does not account for the effect of loading direction on cell rigidity [20].

$$M = s - 3n + 6 \qquad\qquad (1)$$
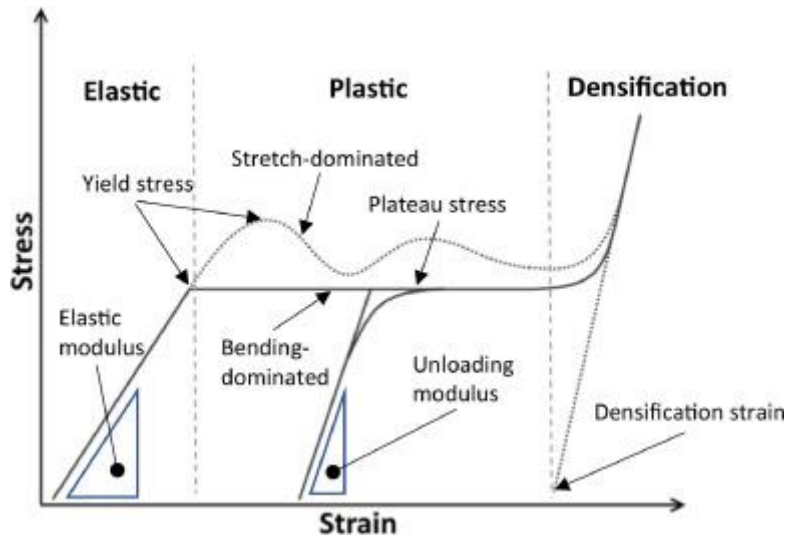
FIGURE 6 - BENDING DOMINATED AND STRETCH DOMINATED STRESS-STRAIN BEHAVIOUR [18]

The relationship between fatigue strength and number of load cycles in a lattice material may be defined according to the typical S-N power law as expressed in Equation 2, where S^* is the fatigue strength and N_f^* is the number of cycles. The coefficient A^* and the exponent b^* are effected by the lattice relative density, the fatigue strength of the bulk material, the cell geometry and the solid distribution [19].

$$S^* = A^* N_f^{*b^*} \tag{2}$$

The fatigue failure of the structure can be modelled as the continuous failure of struts, with the structural stiffness decreasing with each strut failure. The S-N law for individual struts is defined by Equation 3.

$$S_{N_f} = A_s N_f^{b_s} \tag{3}$$

The dependence between the coefficients and exponents of each S-N law can be described by Equations 4 and 5, where C_A and n_A are a function of cell topology and struts' shape and C_b depends on strut irregularities only. The relative density, $\frac{\rho^*}{\rho_s}$, or volume fraction, represents the volume of the lattice cell solid material as a fraction of the volume enclosed by the lattice cell boundary.

$$A^* = C_A A_s \left(\frac{\rho^*}{\rho_s}\right)^{n_A} \tag{4}$$

$$b^* = C_b b_s \tag{5}$$

The macrostructure S-N relation in Equation 2 can therefore be re-written as Equation 6 [19].

10

$$S^* = C_A A_s \left(\frac{\rho^*}{\rho_s}\right)^{n_A} N_f^{*C_b b_s} \tag{6}$$

In an additive manufactured lattice structure, there are numerous additional parameters that could affect fatigue properties of struts. These include the energy input of ray, scanning speed, scanning strategy, the size of particles in powder, the temperature of building chamber and the layer thickness. The layer-by-layer process may also result in new layers causing a heat treatment of previous layers, which could alter the microstructure of struts [19].

2.4. TOPOLOGY OPTIMISATION

Topology optimisation is a developing field of mathematical design simulation for load bearing engineering structures, whereby optimal structural geometries are defined within a design space that satisfy mechanical constraints and boundary conditions whilst minimising a cost function. The method is typically valued for its ability to minimise the weight or compliance of a structure whilst satisfying structural constraints [21]. The density-based topology optimisation approach generally employs the finite method to assign a mesh to the structure and a unique design variable, x_k, for each element of the mesh. The design variable is a pseudo-density parameter that varies between 0 and 1, 0 representing a void and 1 representing solid material at the location of the element [22]. The optimisation results in a material distribution that satisfies performance requirements and constraints given the particular boundary and load conditions. An example of topology optimisation on a component is shown in Figure 7.
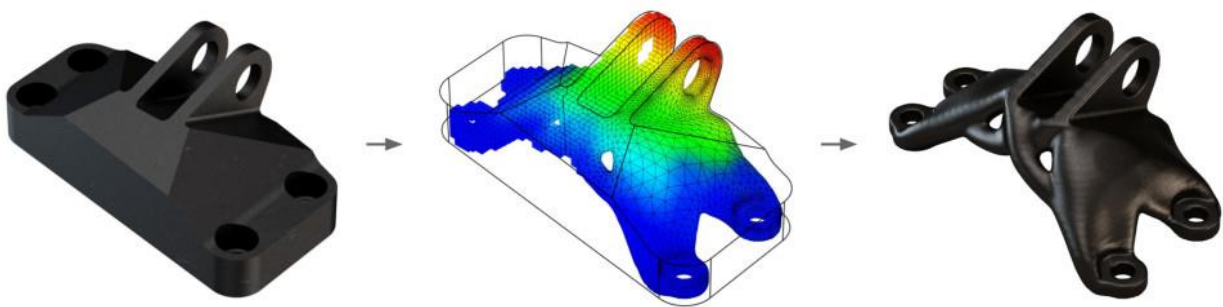

FIGURE 7 - TOPOLOGY OPTIMISATION EXAMPLE

2.4.1. STIFFNESS-MAXIMISING TOPOLOGY OPTIMISATION

The most common use of topology optimisation is in the binary compliance problem. This seeks a solution comprising only of voids or solid material, where stiffness is maximised with weight constraints. Maximising stiffness is equivalent to minimising the work done by the forces applied

to the structure (the compliance). The stiffness is defined by the following fundamental equilibrium equation, where K is the stiffness matrix and F and $U(x)$ are the force and displacement vectors respectively.

$$K\big(\rho(x)\big)U\big(\rho(x)\big) = F \qquad (7)$$

The solid isotropic material penalisation (SIMP) approach is often used in this problem. This approach parameterises the material properties based on the design variables, fitting a power law relation that penalises intermediate density values. As a result, the optimisation process 'pushes' all element design variables to 0 or 1. This can be expressed by either one of the following two schemes (Equations 8a and 8b or Equations 9a and 9b) where K is the stiffness matrix and E is the Young's Modulus [23] [22] [24]. Subscript e refers to element level parameters and q and p are the penalisation factors in the respective schemes, typically set to a value of 3. K_e^0 represents the element stiffness matrix per unit modulus.

$$\eta_K(\rho_e) = \rho_e^q \qquad (8a)$$

$$K(\rho) = \sum_{e=1}^{n_e} \eta_K(\rho_e)K_e \qquad (8b)$$

$$E_e(\rho_e) = E_{min} + \rho_e^p (E_0 - E_{min}) \qquad (9a)$$

$$K(\rho) = \sum_{e=1}^{n} E_e \cdot K_e^0 \qquad (9b)$$

The ρ variable is the 'filtered' design variable. Filtering is a method of weighting design variables by the value of their neighbours as described in Equations 10 and 11 – this reduces mesh size dependancy and removes 'checkerboard patterns' in the resulting optimised structure [25].

$$\rho_e = \sum_{j=1}^{n_e} W_{ej}x_j = \frac{\sum_{k \in \Omega e} w_k x_k}{\sum_{k \in \Omega e} w_k} \qquad (10)$$

$$w_k = \frac{r_0 - r_k}{r_0} \qquad (11)$$

The filtering occurs over a radius r_0, where Ω_e includes all the elements within the radius and w_k is the weight factor for each element within the radius, found from the relative distance of the element to the edge of the filtering radius as demonstrated in Figure 8.
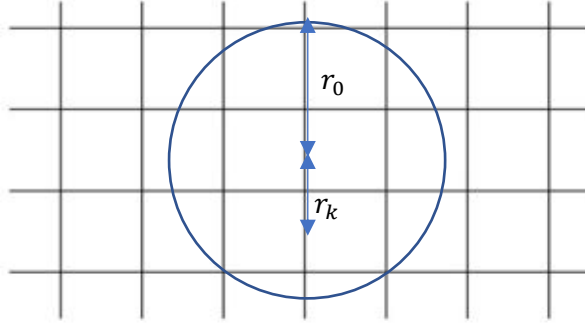
The common compliance minimisation with mass constraint topology optimisation problem formulation can be defined as in Equation 12, where the displacement vector is found from Equation 7 [22]. $\bar{M}$ is the maximum total mass constraint. For a mesh with equally sized elements, the mass constraint can equally be described by an average pseudo-density constraint as in Equation 13.

$$\mathbb{P} = \begin{cases} \min F^T U(x) \\ s.t. \begin{cases} \sum_{e=1}^{n_e} m_e \rho_e(x) \leq \bar{M} \\ 0 < x_e \leq 1 \end{cases} \end{cases} \tag{12}$$

$$\frac{\sum_{e=1}^{n_e} \rho_e(x)}{n_e} \leq \bar{\rho}_{avg} \tag{13}$$

2.4.2. STRESS-CONSTRAINED TOPOLOGY OPTIMISATION

Recently, there has been an increased interest in topology optimisation methods that fulfil stress constraints. Since stiffness maximising topology optimisations do not account for stresses, they may lead to stress concentrations and therefore demand significant adjustment of the resulting topology to achieve a conceptual design. By integrating a stress constraint into the topology optimisation, the resulting topology may be closer to final designs. The objective function in this case may be to minimise mass, or to minimise compliance with a secondary constraint on mass, shown by Equation 14 and 15 respectively, where σ_i^{PN} is the P-norm stress measure for cluster i and $\bar{\sigma}$ is the stress limit [22].

$$\mathbb{P}_1 = \begin{cases} \min \sum_{e=1}^{n_e} m_e \rho_e(x) \\ s.t. \begin{cases} \sigma_i^{PN}(x) \leq \bar{\sigma} \\ 0 < x_e \leq 1 \end{cases} \end{cases} \tag{14}$$

13

$$\mathbb{P}_2 = \left\{ s.t. \left\{ \begin{array}{c} \min F^T u(x) \\ \sigma_i^{PN}(x) \leq \bar{\sigma} \\ \sum_{e=1}^{n_e} m_e \rho_e(x) \leq \bar{M} \\ 0 < x_e \leq 1 \end{array} \right. \right. \tag{15}$$

The P-norm stress measure (Equation 16) is a way of approximating the maximum von mises stress in a defined group of elements Ω_i whilst maintaining differentiability of the stress parameter – a necessary characteristic for sensitivity method optimisation algorithms. This 'clustered' approach seeks to allow for local stress control without the computational expense of evaluating the stress constraint at every element in the structure.

Von mises stresses for each element are found from element principal stresses as in Equation 17. Implicit within most stress vector formulations found in literature is a SIMP approach that applies a penalisation function to the solid material stress vector (Equation 18). As shown in Equation 19, the penalisation function is of an identical form to Equation 8a, but with a typical penalisation factor value of ½ [22]. The SIMP application has the same effect as in the stiffness maximising case of preventing intermediate design variables. From finite element theory, the solid material stress vector in three dimensions is as described in Equation 20. $[C^s]$ is the solid material constitutive relationship matrix and $[B]$ is the dimension matrix, which relates nodal displacements to strains.

$$\sigma_i^{PN} = \left(\frac{1}{N_i} \sum_{a \epsilon \Omega_i} (\sigma_e^{VM})^p \right)^{\frac{1}{p}} \tag{16}$$

$$\sigma_e^{VM} = \left(\sigma_{e_x}^2 + \sigma_{e_y}^2 + \sigma_{a_z}^2 - \sigma_{e_x}\sigma_{e_y} - \sigma_{e_y}\sigma_{e_z} - \sigma_{e_z}\sigma_{e_x} + 3\sigma_{e_{xy}}^2 + 3\sigma_{e_{yz}}^2 + 3\sigma_{e_{xz}}^2 \right)^{\frac{1}{2}} \tag{17}$$

$$\sigma_e = \eta_S(\rho_e)\sigma_e^s \tag{18}$$

$$\eta_S(\rho_e) = \rho_e^p \tag{19}$$

$$\sigma_e^s = [C^s][B][u] = \begin{bmatrix} \sigma_{e_x} \\ \sigma_{e_y} \\ \sigma_{e_z} \\ \sigma_{e_{xy}} \\ \sigma_{e_{xz}} \\ \sigma_{e_{yz}} \end{bmatrix} \tag{20}$$

2.4.3. OPTIMISATION METHODS

There are several optimisation algorithms that may be used in a topology optimisation, with scripts employing methods including sequential quadratic programming, the method of moving asymptotes and the optimality criteria method [26] [22]. These methods generally make use of the adjoint method, which is a way to compute the gradients of the objective function at cost which does not depend upon the number of design variables [27]. Major disadvantages of the sequential quadratic programming method include a lack of robustness and infeasibility caused by the linearisation of the constraint. The optimality criteria method, adopted in the topology optimisation of this project, is a specific case of the method of moving asymptotes, valued for its numerical simplicity and efficiency [26].

3. METHODOLOGY

3.1.   PROBLEM DEFINITION

3.1.1. TOPOLOGY OPTIMISATION APPLICATION METHOD

Following the literature review, the potential benefit of applying topology optimisation to the implant design was confirmed, despite some imposed necessity to deviate from standard methods established in literature.

The application of density-based topology optimisation is attractive in the context of a lattice structure optimisation problem due to the optimisation's use of the pseudo-density filtered design variables, ρ, which are assigned to each element and vary between 0 and 1. These parameters are 'nudged' toward 0 or 1 in conventional binary topology optimisations, where the use of solid material only makes intermediate values redundant, by means of a penalisation function. However, in the case of lattice materials, the filtered design variable is intuitively analogous to local lattice relative density or volume fractions. The topology optimisation application to this structure therefore presents a unique case where intermediate design variable values are both physical and desired. This demanded a deviation from the standard SIMP approach.

The use of topology optimisation demands a mechanical property cost function to minimise and a mechanical property constraint. Ideally, the compromise upon bone remodelling capability of the tibial tray would be minimised, by minimising a cost function describing the deviation of local modulus values from that of the surrounding bone, and stress constraints would be imposed on the structure's maximum von mises stress. This constraint value should strictly be defined

according to the fatigue behaviour of the material. An S-N curve for the material, which may be expressed as in Equation 6, would be the most appropriate way to define this limit, finding the stress threshold below which the 10 million cycles can be survived as demanded by the ISO test. However, this would require significant material testing to establish the coefficients of this equation, accounting for their various dependencies outlined in Section 2.3. Since this process would have been time consuming and the lattice's fatigue behaviour was not the focus of the project, the yield stress was considered as the stress constraint as a first approximation.

Since topology optimisations employing stress constraints are still novel and complex, even more so those implementing non-penalising methods, this ideal topology optimisation case was shelved, with the primary focus instead being dedicated to implementing a non-penalising approach to the standard compliance-minimising, mass-constrained topology optimisation outlined in Section 2.4.1. Data obtained from the Biomechanics Group showed that the modulus values through the structure could be linearly related to the local volume fractions within the volume fraction range shown in Figure 9. Tibial modulus measurements by the Group suggested the left-side tibial tray modulus values shown in Figure 10 for effective modulus matching and bone remodelling. These values would be laterally inverted for a right-side tibial tray.
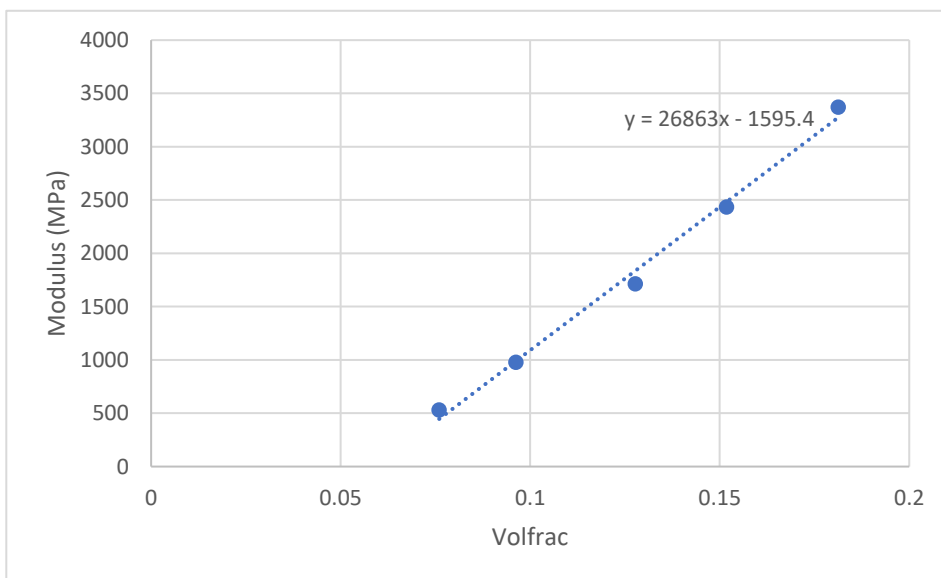

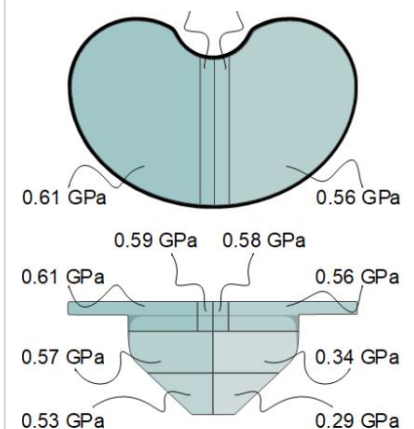FIGURE 9 - MODULUS - VOLUME FRACTION RELATIONSHIP

FIGURE 10 - TARGET MODULUS VALUES FOR EFFECTIVE BONE REGENERATION

These target values and the linear relation could be used to find target volume fraction values as summarised in Table 1.

TABLE 1 - TARGET REGIONAL VOLUME FRACTIONS

Region	Modulus Target (GPa)	Volume Fraction Target
Left 1	0.56	0.080
Left 2	0.34	0.072
Left 3	0.29	0.070
Right 1	0.61	0.082
Right 2	0.57	0.081
Right 3	0.53	0.079

The mass constraint formulation of the compliance minimising topology optimisation described by Equation 13 could therefore be used to impose a constraint on average deviation from effective remodelling performance. The regional differences in modulus targets would necessitate separate constraints being imposed in each region. The compliance minimising objective function was not obviously related to the failure behaviour of the structure, though was suspected to have some benefits. In order to evaluate failures and determine expected ISO test performance, it would be necessary to obtain a global tensor describing the von mises stress distribution through the structure by finite element analysis. This could also be used to adapt the design resulting from the stiffness-based topology optimisation, adjusting the local volume fractions according to which elements are at greatest risk of failure. These will be termed hybrid designs. The methodology process was therefore as described in Figure 11.
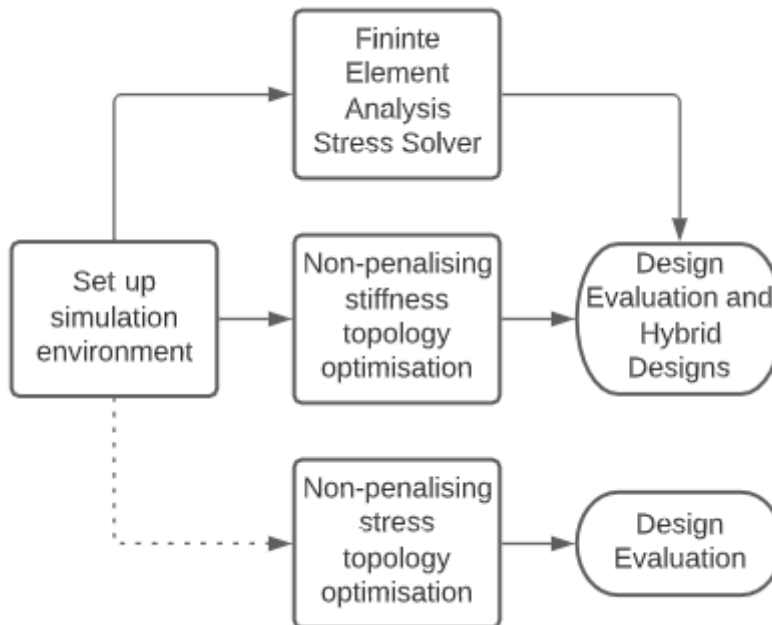

FIGURE 11 - PROJECT METHODOLOGY PROCESS

17

3.1.2. Boundary and Loading Conditions

Setting up the simulation environment was the first step in the project and required the mesh and the boundary and loading conditions to be specified. Since the topology optimisation would have to deviate from standard methods with ad hoc adjustments being made according to the stress distribution, significant customisability was required. MATLAB was therefore used as the simulation environment rather than pursuing topology optimisation solvers built into CAD packages such as Fusion or Solidworks. The *top3d* MATLAB script was used as the starting point for this analysis – a basic and compact SIMP-method binary compliance minimising topology optimisation for a cantilevered beam [26]. A mesh consisting of cubic elements only with adjustable resolution was chosen to minimise the complexity of meshing in MATLAB. The boundary and loading conditions were to be defined in accordance with an ISO test upon a left-side tibial tray as in Figure 10, with a smaller region of tri-directional fixing within the simply supported fixing region to prevent rigid body modes in the solution. Since pure yielding was being considered as opposed to fatigue failure, a static 900 N loading condition was used.
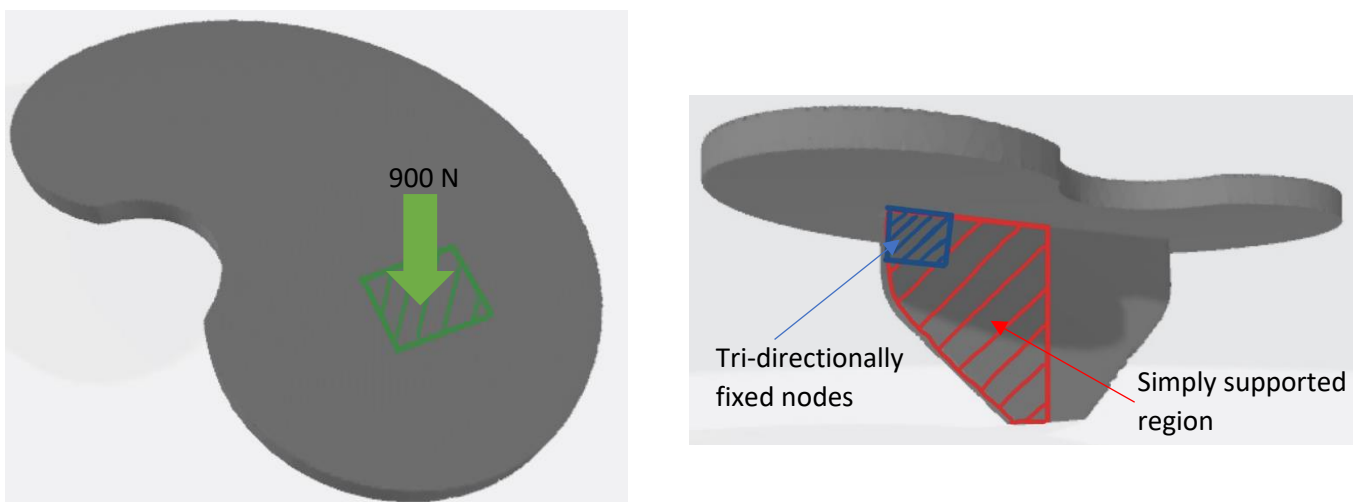
FIGURE 12 - LOADING AND FIXING CONDITIONS

3.2. SETTING UP THE SIMULATION ENVIRONMENT

The input variable for the *top3d* script was the elemental dimensions of the cantilever beam. The initial step was therefore to alter the script such that an STL of the tibial tray structure could be input, returning a mesh of the structure for the topology optimisation to be run on. It was also deemed convenient to be able to define the loading and fixing regions with STL blocks, such that the boundary conditions could be adjusted rapidly and without having to edit the script. These blocks were created within the tibial tray's Rhino CAD model such that their axis positions as well as their sizes could accurately represent the boundary conditions.

3.2.1. STL INCORPORATION

A '*READ_STL*' MATLAB function was incorporated into the script, which returned the maximum and minimum dimension in each axis direction for each of the STL inputs. This was then used to find the number of elements in each direction according to a resolution input parameter (number of elements per mm in each direction). The implant STL's elemental dimensions were then used in the '*VOXELISE*' MATLAB function to create an '*implantRegion*' matrix. This matrix represented a meshing of the of the implant's bounding box with the appropriate element numbers in the respective coordinate axis, defining entries as one where solid material exists for that element and zero otherwise. This is illustrated by Figure 13.
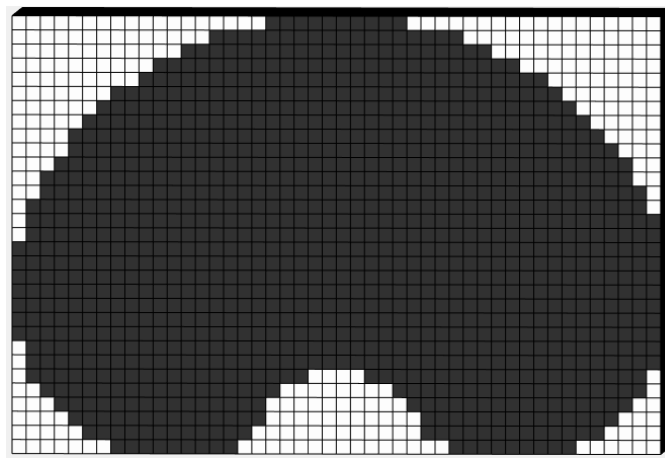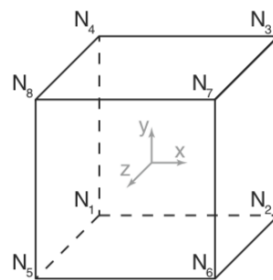

FIGURE 13 - VISUALISATION OF '*IMPLANTREGION*' MATRIX

For the STLs defining the fixing and loading regions, the maximum and minimum coordinate dimensions were used to define offset parameters for each direction, representing the leading

Node Number	Node coordinates	Node ID	Node Degree of Freedoms		
			x	y	z
N_1	(x_1, y_1, z_1)	$NID_1^{\dagger}$	$3*NID_1 - 2$	$3*NID_1 - 1$	$3*NID_1$
N_2	$(x_1 + 1, y_1, z_1)$	$NID_2 = NID_1 + (nely + 1)$	$3*NID_2 - 2$	$3*NID_2 - 1$	$3*NID_2$
N_3	$(x_1 + 1, y_1 + 1, z_1)$	$NID_3 = NID_1 + nely$	$3*NID_3 - 2$	$3*NID_3 - 1$	$3*NID_3$
N_4	$(x_1, y_1 + 1, z_1)$	$NID_4 = NID_1 - 1$	$3*NID_4 - 2$	$3*NID_4 - 1$	$3*NID_4$
N_5	$(x_1, y_1, z_1 + 1)$	$NID_5 = NID_1 + NID_z^{\ddagger}$	$3*NID_5 - 2$	$3*NID_5 - 1$	$3*NID_5$
N_6	$(x_1 + 1, y_1, z_1 + 1)$	$NID_6 = NID_2 + NID_z$	$3*NID_6 - 2$	$3*NID_6 - 1$	$3*NID_6$
N_7	$(x_1 + 1, y_1 + 1, z_1 + 1)$	$NID_7 = NID_3 + NID_z$	$3*NID_7 - 2$	$3*NID_7 - 1$	$3*NID_7$
N_8	$(x_1, y_1 + 1, z_1 + 1)$	$NID_8 = NID_4 + NID_z$	$3*NID_8 - 2$	$3*NID_8 - 1$	$3*NID_8$

$^{\dagger}NID_1 = z_1*(nelx+1)*(nely+1)+x_1*(nely+1)+(nely+1 - y_1)$
$^{\ddagger}NID_z = (nelx+1)*(nely+1)$

FIGURE 14 - NODE AND DEGREE OF FREEDOM LABELLING SCHEME

edge of that STL within the implant's element coordinates. The values were also used to find the fixing and loading STL elemental dimensions. A looping scheme was then used to define the loaded and fixed nodes, which made use of the *'implantRegion'* matrix, fixing and loading offset parameters and the number of elements in each direction for both STLs. This counted through the elements in the *'implantRegion'* matrix coinciding with the regions of the fixing and loading STLs and, if the matrix entry was equal to one (representing the presence of tibial tray material), the nodes of that element were added to an array. This array was then used to define the nodal degrees of freedom that would be fixed or loaded. The *'implantRegion'* matrix was also used in the optimisation section of the script, for zeroing those entries of the volume fraction matrix '*xPhys'*, the compliance sensitivity matrix '*dc'* and the modulus matrix '*E'* corresponding to elements contained within the bounding box of the implant but outside of the implant material.

In defining the loaded and fixed degrees of freedom of the structure, and in assembling the global stiffness matrix, the node labelling scheme defined in *top3d* was adopted. This can be described by Figure 14 – finding the coordinates of an element's corner node closest to the global origin, N_1, allows all other element node IDs and degree of freedom IDs to be found.

Once the STL incorporating edits had been made, STLs defining the default beam dimensions and fixing and loading boundary conditions of the original *top3d* script were input to validate the adjusted script. The binary compliance method topology optimisation result was reproduced successfully as seen in Figure 15. The rotated orientation following the adjustments was a result of the *top3d* script and the *READ_STL* function defining the y and z directions inversely.
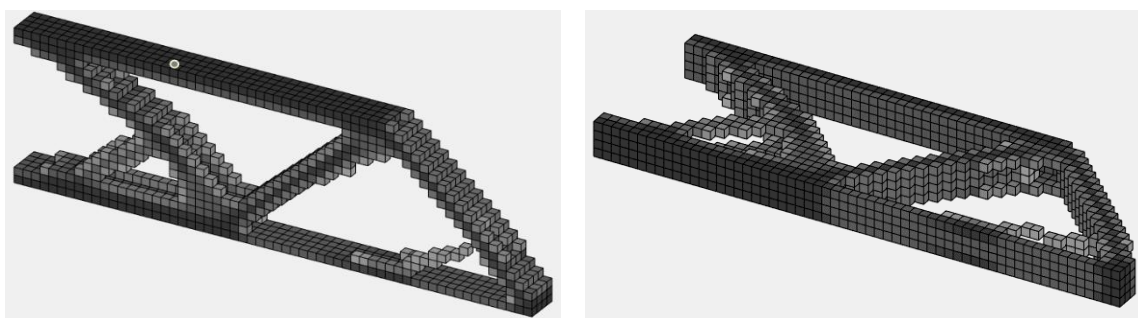

FIGURE 15 – LEFT: RESULT FROM RUNNING DEFAULT '*TOP3D'*; RIGHT: RESULT FROM RUNNING MODIFIED SCRIPT WITH APPROPRIATE STL INPUTS

Running the script on the implant STL with the respective loading and fixing region STLs at this stage gave the result shown in Figure 16.
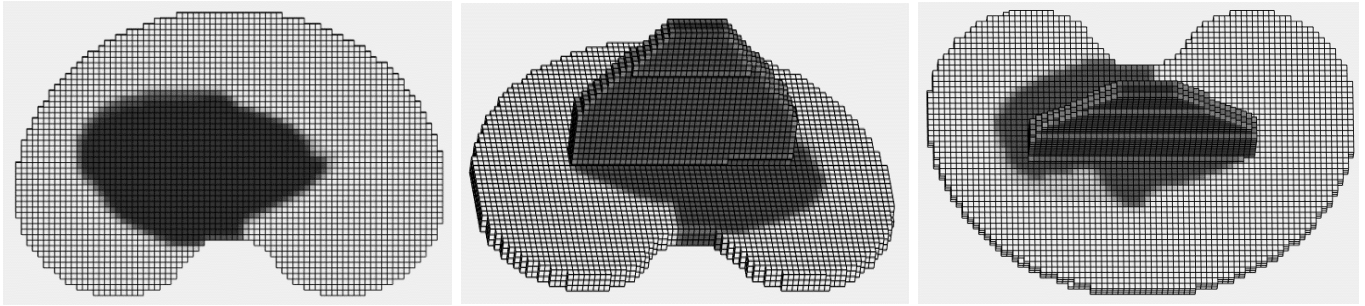
FIGURE 16– TOPOLOGY OPTIMISATION RESULT AFTER STL IMPLEMENTATION

3.3. DEVELOPING A NON-PENALISING STIFFNESS TOPOLOGY OPTIMISATION

3.3.1. REGIONALISATION

The modulus targets for effective bone regeneration were regional dependant, as described in Figure 10. To define these regions in the *'implantRegion'* matrix, STLs of each region's bounding box were made and *'READ_stl'* was used again to define the regions' maximum and minimum element locations within the implant in a similar fashion to the definition of the fixing and loading element offset parameters. At the optimisation stage, these parameters were used to 'split' the volume fraction and compliance sensitivity matrices, capturing the region of interest only. The optimisation loop was then run for each one of these regions in turn using the relevant volume fraction constraint before 'stitching' the regional *'xPhys'* matrices back together into a global *'xPhys'* once again. The optimality criteria adjoint optimisation algorithm adopted from *top3d* is demonstrated by the algorithm flowchart in Figure 17. The optimisation makes use of the Lagrange function formulation of the compliance minimisation problem with average volume fraction constraints show in Equation 21. In particular, this is reformulated as in Equation 22, defining a variable Be which should equal one if the optimisation is satisfied. This parameter is used to 'nudge' the design variables in the appropriate direction, using a *'move'* parameter defining the maximum change per iteration of the optimisation loop. A bi-sector method is then used to adjust the Lagrange multiplier within a domain range according to the volume fraction constraint. Since the compliance sensitivity matrix is found before running the optimisation loop based upon the design variable matrix result from the previous iteration, the approach of running separate optimisations on each region in turn was deemed acceptable.

$$\mathbb{P} = \begin{cases} min\ c(\rho) = F^T u(x) \\ s.t. \begin{cases} \dfrac{\sum_{e=1}^{n_e} \rho_e(x)}{n_e} \leq \bar{\rho}_{avg} & \rightarrow \dfrac{\partial c(\rho)}{\partial x_e} + \lambda \dfrac{\partial \rho_{tot}}{\partial x_e} = 0 \\ 0 < x_e \leq 1 \end{cases} \end{cases} \tag{21}$$

$$Be = -\frac{\partial c(\rho)}{\partial x_e}\left(\lambda \frac{\partial \rho_{tot}}{\partial x_e}\right)^{-1} = 1 \qquad (22)$$
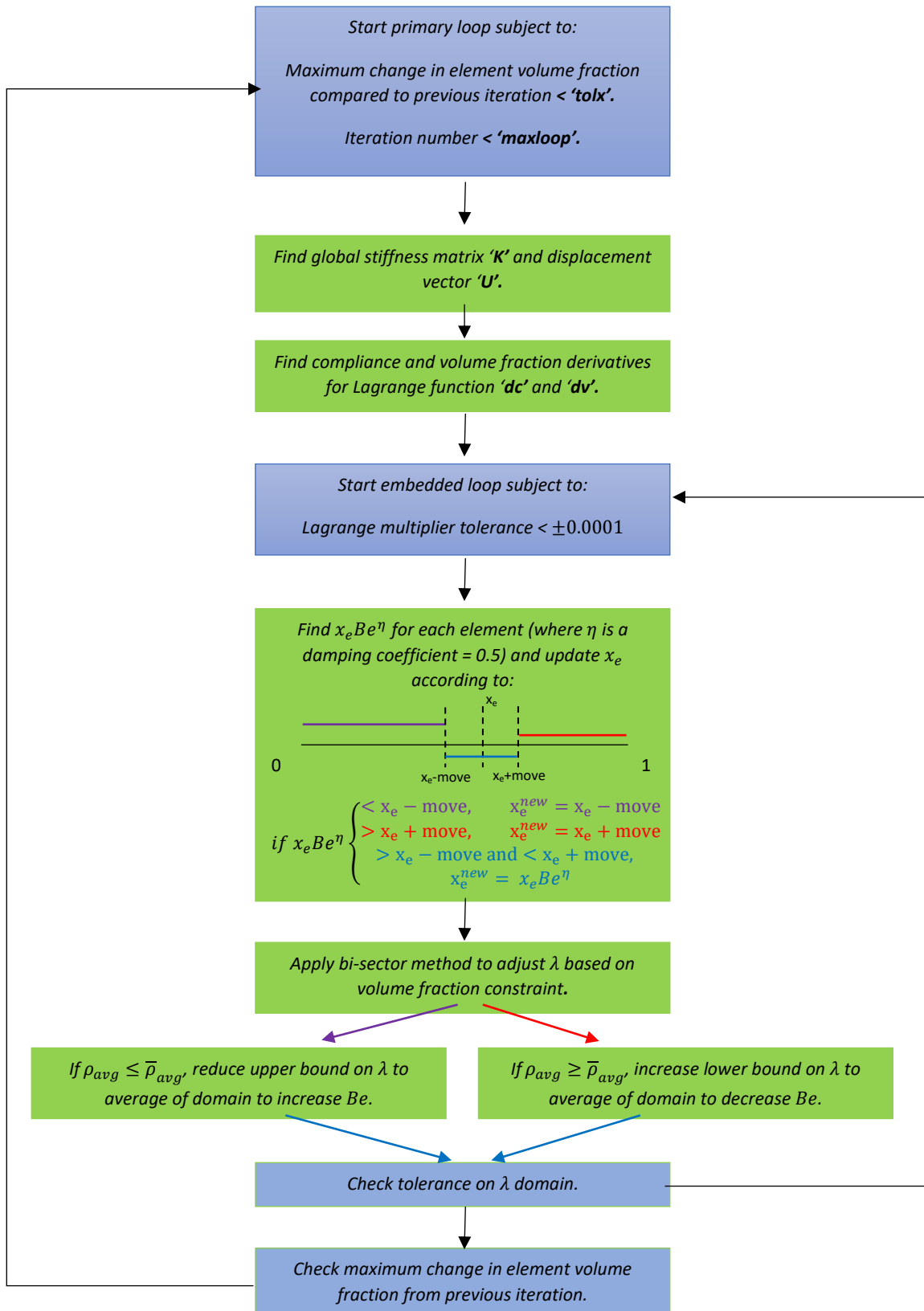

FIGURE 17 – OPTIMALITY CRITERIA METHOD ALGORITHM FLOWCHART

3.3.2. Non-Penalising Stiffness matrix

The assembly of the structure's global stiffness matrix used the method described by Equation 9b in Section 2.4.1, reproduced below.

$$K(\rho) = \sum_{e=1}^{n} E_e \cdot K_e^0$$

The unit modulus element stiffness matrix K_e^0 was assembled using the finite element method (Equation 23), taking a volume integral of the matrix multiple of B^T, C^0 and B using the Gauss integration method. This was a [24 x 24] matrix since each element had 8 nodes each with 3 degrees of freedom. The matrix was also identical for all elements since the element shape and sizes were identical, and the element modulus was the only parameter with functional dependence upon the element volume fraction. $[C^0]$ is the standard constitutive matrix per unit modulus for a hexahedron element described by Equation 25, where v is the material's Poisson's ratio, and $[B]$ is the dimension matrix relating the element's nodal displacement vector to the nodal strains by taking the required derivatives of the shape functions, $N_1 - N_8$ as in Equation 24. These shape functions define the relationship between nodal displacements and the displacements through the element, illustrated by Figure 18. At the coordinates of each node, the shape function of that node becomes equal to 1 and all others are equal to 0.

$$[K^0] = \int B^T C^0 B \, dVol \qquad (23)$$

$$[B] = \begin{bmatrix} \frac{\partial}{\partial x} & 0 & 0 & \frac{\partial}{\partial y} & 0 & \frac{\partial}{\partial z} \\ 0 & \frac{\partial}{\partial y} & 0 & \frac{\partial}{\partial x} & \frac{\partial}{\partial z} & 0 \\ 0 & 0 & \frac{\partial}{\partial z} & 0 & \frac{\partial}{\partial y} & \frac{\partial}{\partial x} \end{bmatrix}^T \begin{bmatrix} N_1 & 0 & 0 & N_2 & 0 & 0 & \dots & N_8 & 0 & 0 \\ 0 & N_1 & 0 & 0 & N_2 & 0 & \dots & 0 & N_8 & 0 \\ 0 & 0 & N_1 & 0 & 0 & N_2 & \dots & 0 & 0 & N_8 \end{bmatrix} \qquad (24)$$

$$[C^0] = \frac{1}{(1+v)(1-2v)} \times \begin{bmatrix} 1-v & v & v & 0 & 0 & 0 \\ v & 1-v & v & 0 & 0 & 0 \\ v & v & 1-v & 0 & 0 & 0 \\ 0 & 0 & 0 & \frac{1-2v}{2} & 0 & 0 \\ 0 & 0 & 0 & 0 & \frac{1-2v}{2} & 0 \\ 0 & 0 & 0 & 0 & 0 & \frac{1-2v}{2} \end{bmatrix} \qquad (25)$$
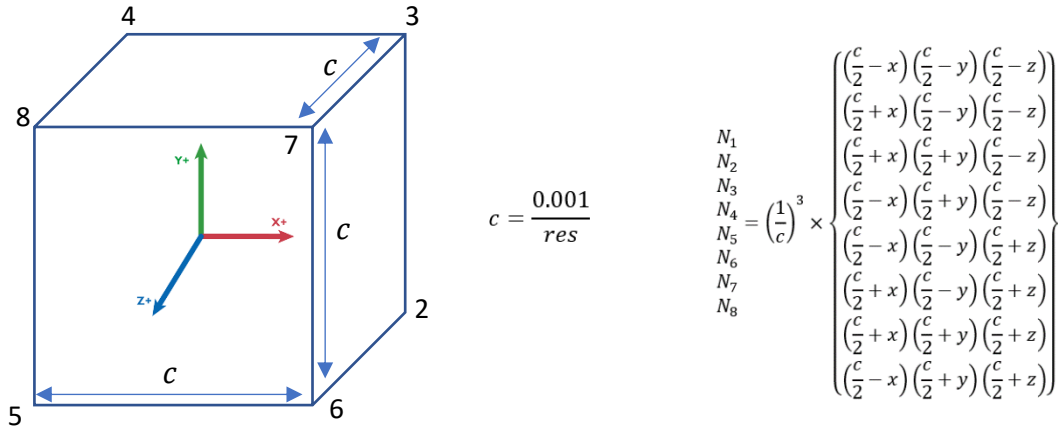
FIGURE 18 - ELEMENT SHAPE FUNCTIONS

$$c = \frac{0.001}{res}$$

$$\begin{Bmatrix} N_1 \\ N_2 \\ N_3 \\ N_4 \\ N_5 \\ N_6 \\ N_7 \\ N_8 \end{Bmatrix} = \left(\frac{1}{c}\right)^3 \times \begin{Bmatrix} \left(\frac{c}{2}-x\right)\left(\frac{c}{2}-y\right)\left(\frac{c}{2}-z\right) \\ \left(\frac{c}{2}+x\right)\left(\frac{c}{2}-y\right)\left(\frac{c}{2}-z\right) \\ \left(\frac{c}{2}+x\right)\left(\frac{c}{2}+y\right)\left(\frac{c}{2}-z\right) \\ \left(\frac{c}{2}-x\right)\left(\frac{c}{2}+y\right)\left(\frac{c}{2}-z\right) \\ \left(\frac{c}{2}-x\right)\left(\frac{c}{2}-y\right)\left(\frac{c}{2}+z\right) \\ \left(\frac{c}{2}+x\right)\left(\frac{c}{2}-y\right)\left(\frac{c}{2}+z\right) \\ \left(\frac{c}{2}+x\right)\left(\frac{c}{2}+y\right)\left(\frac{c}{2}+z\right) \\ \left(\frac{c}{2}-x\right)\left(\frac{c}{2}+y\right)\left(\frac{c}{2}+z\right) \end{Bmatrix}$$

The global stiffness matrix was then assembled by multiplying the element stiffness matrix by each element's modulus value in turn, before positioning the entries in the global matrix according to the 24 degree of freedom IDs of that element. By replacing the SIMP modulus – volume fraction relationship with the empirical relationship established in Figure 9 and zeroing all values for elements not in the implant region, the non-penalising method was established.

A scaling described by Equation 26 and Table 2 was applied to the volume fraction constraints at the start of the script. There were several reasons for this. Firstly, as seen in Figure 9, a minimum bound on the allowable volume fraction was needed to limit the extrapolation of the linear trend and to prevent non-physical tiny or negative values. Since the lowest average volume fraction target was 0.070, the scaling set the minimum volume fraction to 0.060 to allow a sufficient domain in which element volume fractions in this region could fall below the target average during the optimisation without the extrapolation errors mentioned. An upper bound of 0.1 was selected to set a range of allowable volume fractions that would not result in individual elements deviating too far from their regional target. If all elements varied drastically from the regional targets despite the average regional volume fraction constraint being satisfied, the constraint would be redundant in terms of maintaining bone remodelling properties. The scaling also allowed for sufficient precision in the design variable adjustments during the optimisation whilst using a *'move'* value of 0.1, which had favourable convergence and run time performance. The scaling was set to comply with additive manufacturing capabilities, with the chosen volume fraction range lying within that which can easily be created by selective laser manufacture.

$$x = \frac{x_{unscaled} - 0.06}{0.1 - 0.06} \tag{26}$$

TABLE 2 - SCALED VOLUME FRACTION TARGETS

Region	Volume Fraction Target	Scaled Volume Fraction Target
Left1	0.080	0.506
Left2	0.072	0.301
Left3	0.070	0.255
Right1	0.082	0.552
Right2	0.081	0.515
Right3	0.079	0.478

The modulus – volume fraction relationship used (Equation 27) accounted for this scaling.

$$E = (26863 \times [(0.1 - 0.06)x + 0.06] - 1595.4) \times 10^9 \qquad (27)$$

The topology optimisation result was as shown in Figure 19. The region of low volume fractions highlighted appeared due to the region of tri-directional fixing being directly below it.
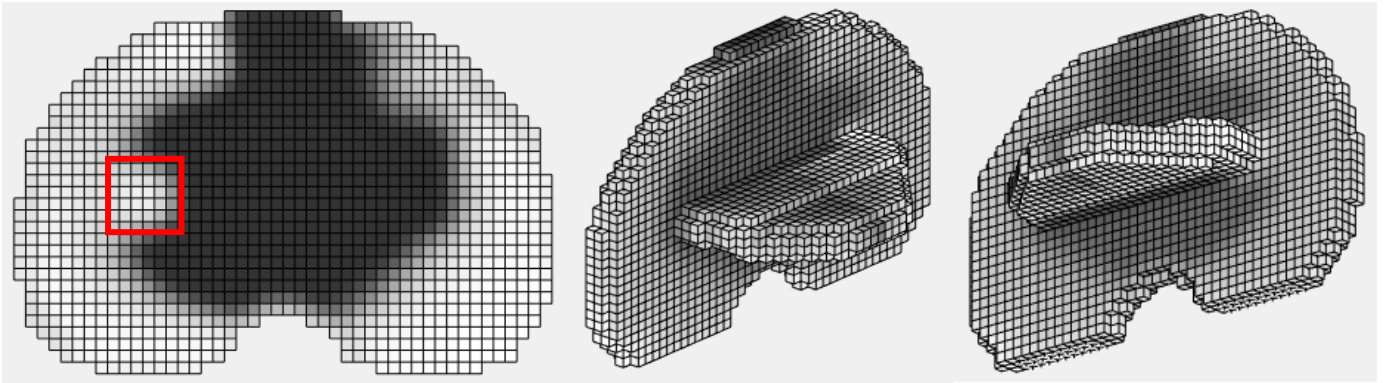

FIGURE 19 – TOPOLOGY OPTIMISATION RESULT AFTER REGIONALISATION AND MODULUS RELATION IMPLEMENTATION

3.4. DEVELOPING A STRESS SOLVER

The stress solver was built in MATLAB to allow stress solutions based on the topology optimisation design to be found and appropriate adjustments to be made easily and rapidly.

3.4.1. FINDING STRESSES AND VALIDATION

The 6-component stress vector for each element was found from the finite element method as in Equation 28, where $[u_e]$ is the 24-component element displacement vector.

$$\sigma_e = [C^0][B][u_e] \cdot E(\rho) = \begin{bmatrix} \sigma_x \\ \sigma_y \\ \sigma_z \\ \sigma_{xy} \\ \sigma_{yz} \\ \sigma_{xz} \end{bmatrix} \qquad (28)$$

25

A cantilever beam example with parameters shown in Figure 20 was considered, and hand calculations were done to find expected values for both wall stress and beam end displacement as in Equations 29 and 30 in order to validate the stress vector formulation as well as the global stiffness matrix formulation described previously. The stress and displacement values obtained from the script matched these within an acceptable error as shown in Table 3.
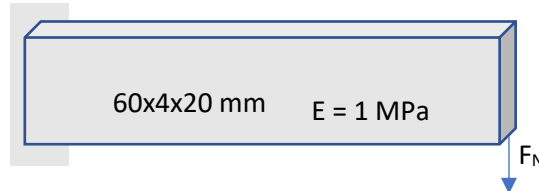

FIGURE 20 – CANTILEVER BEAM CASE USED FOR VERIFICATION

$$u = \frac{1}{EI}\left(0.03F_N x^2 - \frac{1}{6}F_N x^3\right) \tag{29}$$

$$\sigma_x = \frac{My}{I} \tag{30}$$

TABLE 3 – COMPARISON OF HAND CALCULATED PARAMETERS WITH THOSE OBTAINED FROM SCRIPT

	Hand Calc. Value	Value from Script	Error
End u, $F_N = 5N$	0.135 m	0.152 m	12.6%
Built in max σ_x, $F_N = 5N$	-1.13 MPa	-1.26 MPa	11.5%
Built in max σ_x, $F_N = 90N$	-20.25 MPa	-22.66 MPa	11.9%

3.4.2. LOCATION OF STRESS EVALUATION

The element stress vectors were a function of the local element coordinates owing to the functional dependence on $[B]$ (the quoted stress values in Table 3 were evaluated at the element centre). Though the stress values are most accurately obtained at the Gauss points, the degree to which the stress varied through an element was investigated. Figures 21 and 22 below capture the variation of the direct stresses when evaluated at the centre, each of the element nodes and each of the element Gauss points for the cantilever beam element and the three implant elements indicated. The results showed significant variation (more so for the nodal stress evaluations as expected). However, the average of the stresses evaluated at each of the Gauss points, as well as the average of the stresses evaluated at each of the nodes, was equal to the stresses evaluated at

the centre of the element for all cases. It was therefore decided that stress vectors could reasonably be evaluated at the centre of the element concerned.
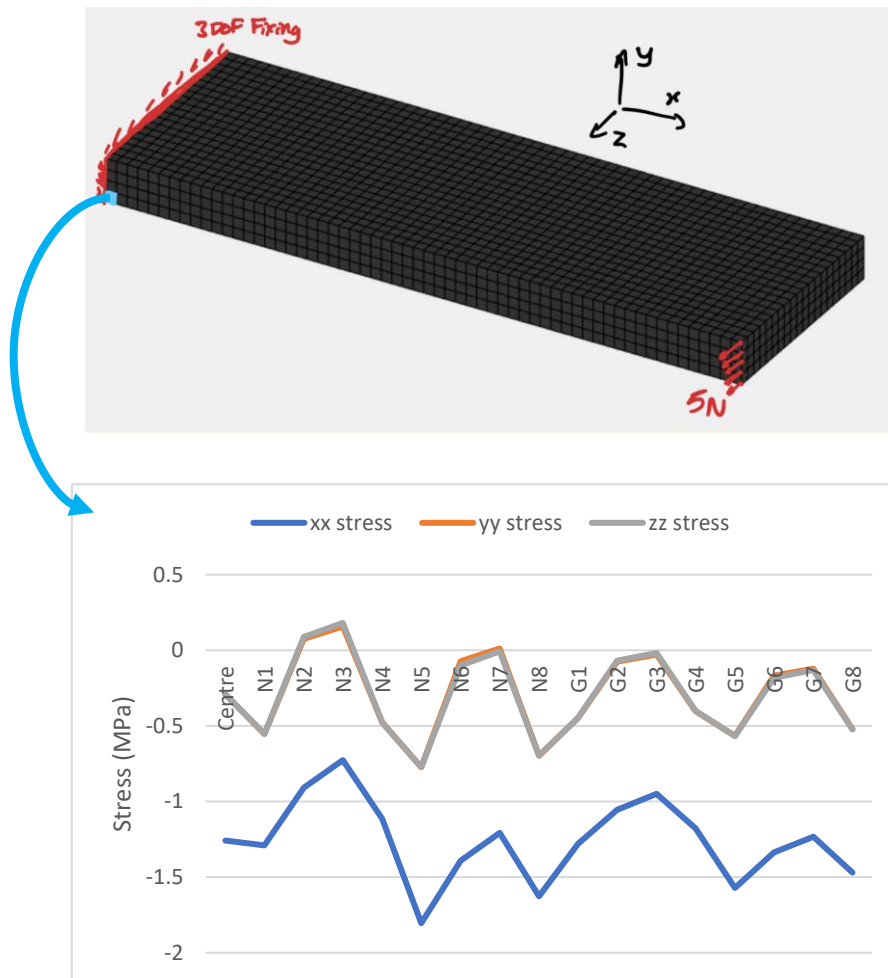

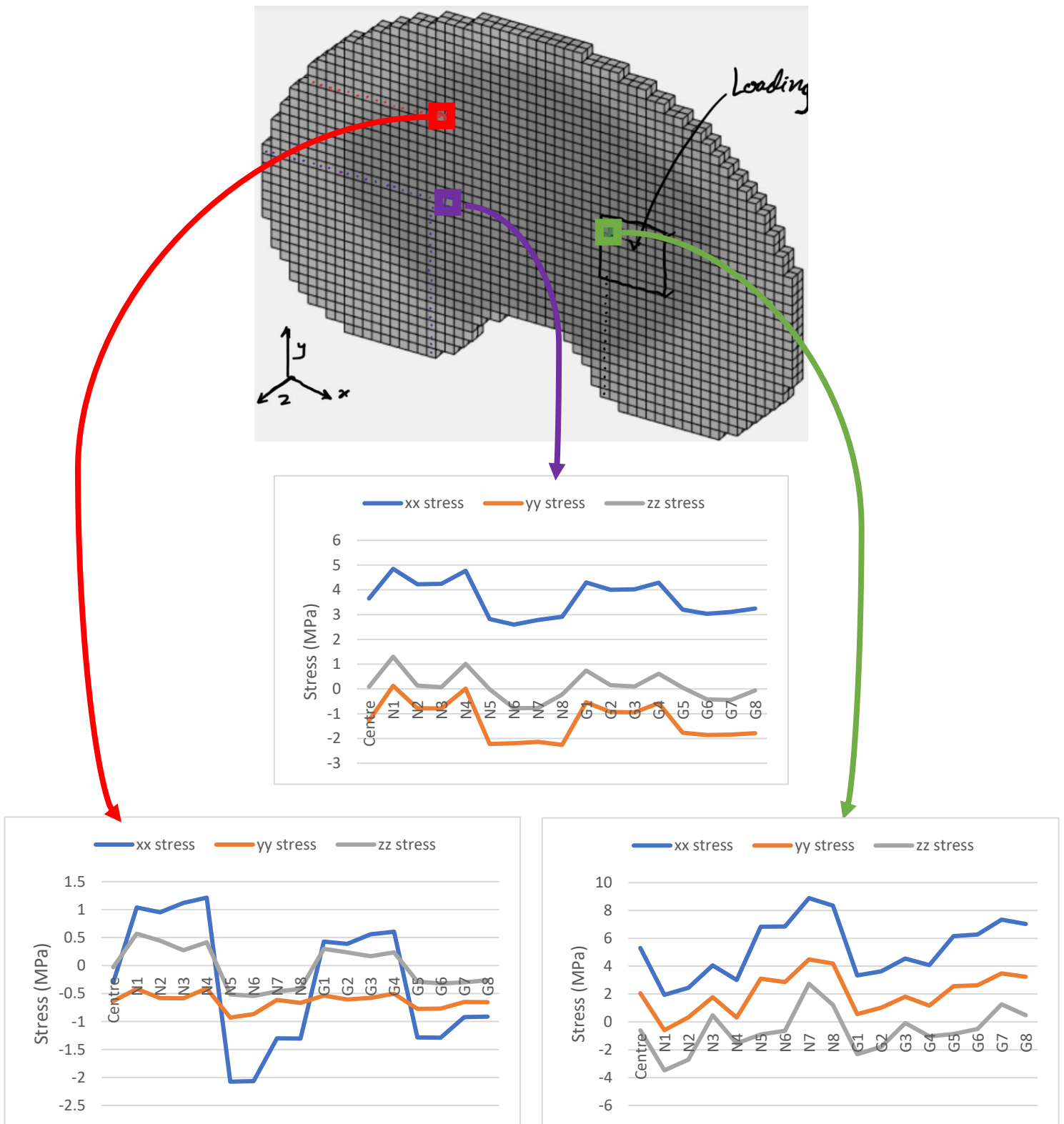FIGURE 21 – VARIATION OF DIRECT STRESSES IN CANTILEVER BEAM ELEMENT SHOWN

FIGURE 22 – VARIATION OF DIRECT STRESSES IN IMPLANT ELEMENTS SHOWN

3.4.3. FAILURE ANALYSIS

A global stress matrix of σ^{VM} values was found by applying Equation 17 to each of the elements after calculating the element stress vector. The yield criterion could then be evaluated as in Equation 31 to determine which elements of the implant mesh were predicted to experience

failure. The yield stress of the lattice material was dependent upon the volume fraction – the trend in Figure 23 was drawn using data obtained from the Biomechanics Group.
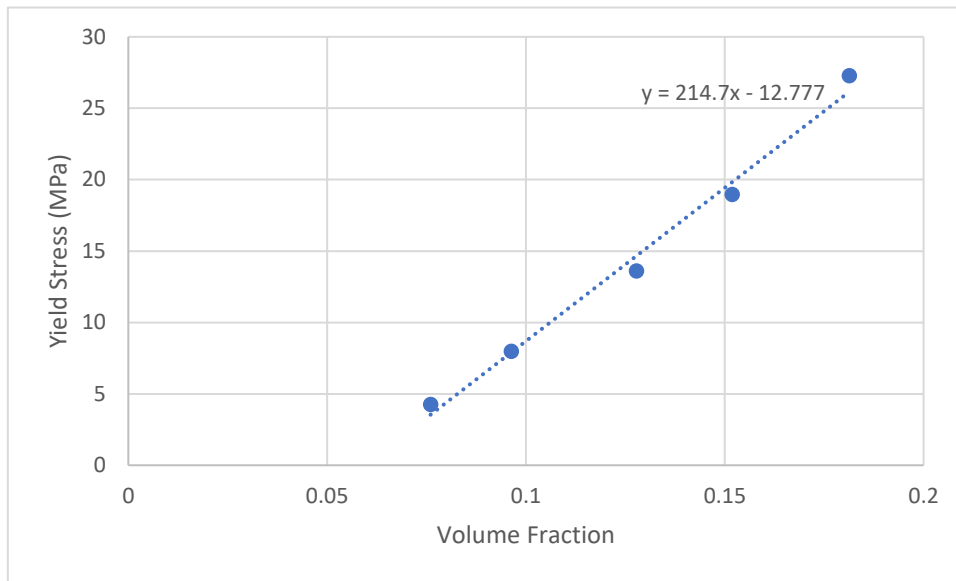

$$\text{FIGURE 23 – YIELD STRESS – VOLUME FRACTION RELATIONSHIP}$$

$$\sigma^{VM} > \sigma^{yield} \tag{31}$$

The stress distribution, failure behaviour and the closeness to modulus targets in the topology optimised design could be compared to a '*Control*' design shown in Figure 24, where all volume fractions were set to their region target values to achieve perfect bone modulus matching, therefore maximising remodelling capability. Comparisons could also be made to a solid structure where all volume fractions were set to 1 with all element moduli set to 110 GPa. This represents the current standard use tibial trays; the other extreme to the *'Control'* design, with perfect strength capabilities but poor bone remodelling capabilities.
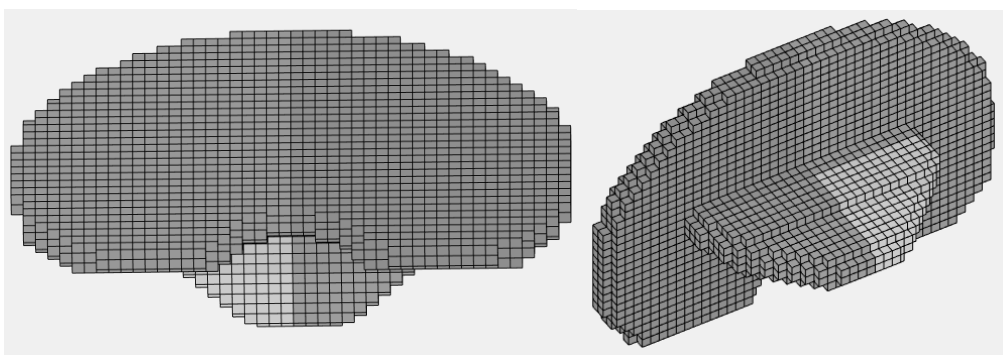

FIGURE 24 – FULLY MODULUS-MATCHED *'CONTROL'* DESIGN

3.5. STRESS SATISFYING HYBRID DESIGNS

Having established the element stresses experienced by the stiffness topology optimisation design, it was possible to create an alternative design that matched each element's yield stress to

its experienced stress. This was done by setting volume fractions using the trend in Figure 23, according to the von mises stress in that element. This design was termed *'Stress Limited'.* This could then be paired with the *'Stiffness Top Op'* design, to create a hybrid design that increased the volume fraction of all elements predicted to fail to their corresponding *'Stress Limited'* value. The resulting design was termed *'Stress Limited Top Op'.* An identical process was followed for the *'Control'* design to create a *'Stress Limited Control'* design.

Each of these three stress limited designs were expected to predict no failures, since the volume fractions had been adjusted for this express purpose. Nevertheless, despite a lower number of element failures being predicted in each of the three designs than both the *'Stiffness Top Op'* and *'Control'* designs, the value was non-zero for each. This was due to the change in the structure's volume fraction distribution causing a change in the structure's stress distribution as summarised in Figure 25. This meant that the '*Stress Limited'* and hybrid designs' attempt at complete failure prevention based upon the '*Stiffness Top Op'* design's stress distribution was partly invalidated. The dependence of the stress distribution upon the volume fraction distribution is worth exploring further at this point.
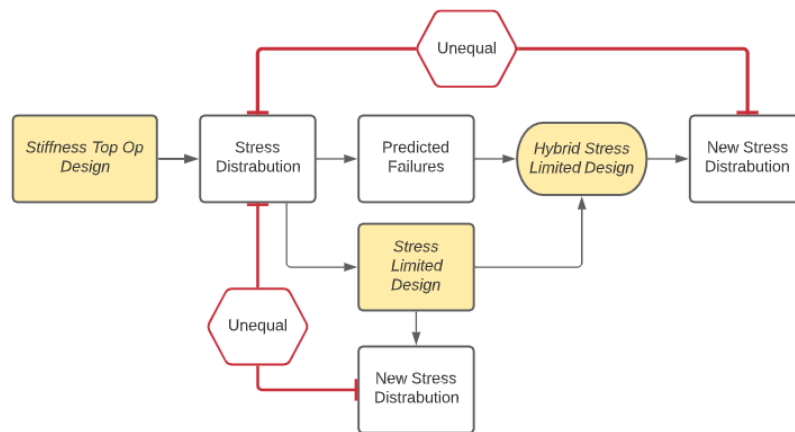

FIGURE 25 – DEFICIENCY OF STRESS LIMITING AND HYBRID APPROACH FOR REMOVING ANY PRECITED FAILURES

3.5.1. UNDERSTANDING THE STRESS – VOLUME FRACTION RELATIONSHIP

Upon initial consideration, it was thought that the stress distribution should have no functional dependence on the volume fraction. This was suggested by considering the element stress vector equation (Equation 28) with the element level application of the force-displacement equation (Equation 7), leading to the following derivation:

$$\sigma_e = [C^0][B][u_e] \cdot E(\rho) = [C^0][B][K_e]^{-1}[F_e] \cdot E(\rho)$$

$$= [C^0][B][K_e^0 \cdot E(\rho)]^{-1}[F_e] \cdot E(\rho) = [C^0][B][K_e^0]^{-1}[F_e] \neq f(\rho)$$

However, it was realised that the element displacement vector could not be considered as the solution of an element level force-displacement equation, as this would negate the effect of the surrounding elements. In the case that an element's volume fraction remains unchanged whilst the surrounding elements' volume fractions change, the $[u_e]$ component of the element's stress vector will change whilst $E(\rho)$ will not. This demonstrates the dependence of all individual element stresses upon the global volume fraction distribution. It should be noted that this verifies the possibility of conducting a non-penalising stress topology optimisation. Whereas penalising stress topology optimisations impose a penalising function, $\eta_S(\rho_e)$, on the solid stress vector, which establishes a functional dependence of the stress upon the volume fraction, a non-penalising case demands a true physical relationship, similarly to how the non-penalising stiffness topology optimisation used the empirical modulus – volume fraction relation. The confirmation of this relation proves a non-penalising stress topology optimisation possible.

3.5.2. CONVERGENT STRESS LIMITED

To improve upon the stress limited designs, a script was written to loop the stress limited volume fraction adjustment process until convergence. The convergence criterion was that no elements should be predicted to fail subject to the required failure-preventing volume fraction adjustment not exceeding 0.2 – the maximum volume fraction that could be produced by the additive manufacture process. This is described by Figure 26. The process was highly sensitive to the initial condition. The *'Convergent Stress Limited'* design was obtained from this process having set an initial design where all element volume fractions were 0.08, the average of the regional targets, to minimise the consequent deviation from these targets. Upon convergence, 12.0% of the tibial tray elements were still predicted to fail, though this represented an improvement upon all designs created previously. Increasing the initial condition continuous volume fraction progressively reduced the number of remaining element failures following the optimisation. A minimum continuous volume fraction initial condition of 0.17 was needed for no element failures to be predicted by the script, although no adjustment was made by the script in this case – the initial condition itself did not contain any predicted element failures. Non-continuous volume fraction distributions in the initial condition were explored by assigning random values to all elements between 0.08 and 0.2, which converged to a design where only 1.24% of elements were predicted to fail.
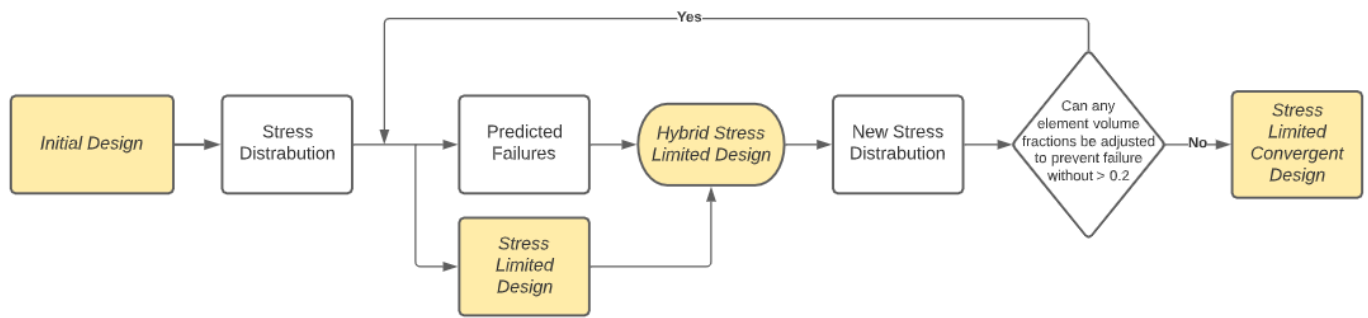
3.6.   DEVELOPING A NON-PENALISING STRESS TOPOLOGY OPTIMISATION

Creating the stress limited and hybrid designs revealed a complicated relationship between the volume fraction distribution and the material stresses. This evidenced the utility of a stress-based topology optimisation, which had the potential to achieve the project aim elegantly and in the most explicit manner – ensuring sufficient tibial tray strength against failure whilst maintaining bone remodelling capability as much as possible. Though the optimisation process would have to be adjusted from the non-penalising stiffness topology optimisation developed previously, the optimality criteria approach would be adopted, as this would provide a well-understood framework. The cost function to be minimised in this case was the deviation of the regional volume fractions from their targets. This was simplified as the minimisation of the sum of the volume fractions, since any stress satisfying design was expected to demand all elements to have higher volume fractions than their regional target. The constraint of each element's experienced von mises stress being below its yield stress found from the trend in Figure 23 was initially considered. However, this was rejected since it would have required a separate optimisation to be run for each element, which would have been highly computationally expensive and inefficient. An alternative constraint formulation would be to keep the maximum von mises stress below a constant yield stress value. A 4.4 MPa yield stress (corresponding to a volume fraction of 0.08) was considered, since the optimised design was not expected to contain any element volume fractions lower than this value. However, it was suspected that this tight constraint might make the optimisation unsolvable and was likely to be unnecessarily conservative. In a structure where the volume fractions vary from 0.08 to 0.2 for example, it is possible (though not certain) that no element failures will occur when a yield stress corresponding to a 0.15 volume fraction is chosen in the maximum stress constraint. Nevertheless, this is contingent upon the elements with volume fractions below 0.15 each having von mises stress values sufficiently below the maximum to also be below that element's yield stress. Selecting the yield stress value was therefore non-trivial.

3.6.1. CLUSTERED STRESS APPROACH

Another issue with the constraint function was the use of the maximum von mises stress. This was unsuitable since the adjoint method optimisation would require the derivatives of the cost and constraint functions to be taken, and the maximum function is non-differentiable. As mentioned in Section 2.4.2, a clustered stress approach is taken to overcome this, as described by the P-norm stress in Equation 16, reproduced below.

$$\sigma_i^{PN} = (\frac{1}{N_i} \sum_{a \epsilon \Omega_i} (\sigma_a^{VM})^p)^{\frac{1}{p}}$$

The p exponent is critical in determining what the P-norm stress of the cluster represents. A P-norm stress with $p = 1$ represents the mean von mises stress whereas one with $p = \infty$ represents the maximum von mises stress (since p must be less than this value to ensure differentiability, the P-norm stress will always be lower than the maximum stress for the cluster). Literature recommends a p value of 8 for the stress constrained topology optimisation to avoid numerical problems. The total number of clusters, n_i, and the distribution of elements contained within each cluster, Ω_i, also effects the stress measure. Setting the number of clusters equal to the number of elements eliminates the computational advantage of not imposing separate constraints on each element. Using only one cluster on the other hand is too rough of an approach and ignores the distribution of stresses. With a resolution of 0.6 elements per mm, the implant contained 4514 elements, for which 50 clusters were used. The local stresses contained within each cluster is best approximated by assembling clusters that group elements with similar stress levels. Therefore, upon each iteration of the optimisation, the elements were organised in order of descending von mises stresses. Once in this order, elements were assigned in turn to a cluster until it was filled before filling the next cluster. Each cluster was of equal size $\frac{n_a}{n_i}$ apart from the last cluster which was smaller. This approach is summarised in Figure 27. A significant advantage of this approach is that the stress constraint of each cluster could be made equal to the yield stress corresponding to the lowest volume fraction within that cluster. This would solve the aforementioned issue related to overly conservative constraints.

$$\underbrace{\sigma_1 \geq \sigma_2 \geq \sigma_3 \geq \ldots \geq \sigma_{\frac{n_a}{n_i}}}_{\text{cluster 1}} \geq \underbrace{\ldots \geq \sigma_{\frac{2n_a}{n_i}}}_{\text{cluster 2}} \geq \ldots \geq \sigma_{\frac{(n_i-1)n_a}{n_i}} \geq \underbrace{\ldots \geq \sigma_{n_a}}_{\text{cluster } n_i}$$

FIGURE 27 – CLUSTERING SCHEME

3.6.2. P-NORM STRESS SENSITIVITY DERIVATION

The problem formulation could be written as follows. A separate optimisation would be conducted for each stress cluster, adjusting the constraint accordingly.

$$\mathbb{P} = \begin{cases} min \sum_{e=1}^{n_e} \rho_e(x) \\ s.t. \begin{cases} \sigma_i^{PN}(x) \le \bar{\sigma_i} \\ 0 < x_e \le 1 \end{cases} \end{cases}$$

Following the optimality criteria method applied to the stiffness topology optimisation, this was written in terms of a reformulated Lagrange function as in Equation 32, to define an optimisation satisfaction parameter, Be, for each element.

$$Be = -\frac{1}{\lambda} \frac{\left(\frac{\partial \rho_{tot}}{\partial x_b}\right)}{\left(\frac{\partial \sigma_i^{PN}}{\partial x_b}\right)} \tag{32}$$

This was to be used in assembling a global sized Be matrix for the cluster, which could then 'nudge' each element's design variable in the appropriate direction before adjusting the Lagrange multiplier using the bisector method as described by Figure 17. The stress topology optimisation simulation would therefore be essentially identical to the stiffness topology optimisation following the computation of the global Be matrices, with a separate optimisation being conducted upon each stress cluster using appropriate stress constraints.

As with the stiffness topology optimisation, the global $\frac{\partial \rho_{tot}}{\partial x}$ matrix consisted of ones everywhere in the implant space since each entry was the sum of that element's filter weighting value contributions for all volume fractions. From the definition of the filter described in Section 2.4.1., this is always equal to 1. This is summarised below.

$$\frac{\partial \rho_{tot}}{\partial x_b} = \sum_{e}^{n_e} \frac{\partial \rho_e}{\partial x_b} = \sum_{e}^{n_e} W_{eb} = 1$$

Calculating the $\frac{\partial \sigma_i^{PN}}{\partial x_b}$ value of each element to assemble the global $\frac{\partial \sigma_i^{PN}}{\partial x}$ matrix was complex, since σ_i^{PN} depended upon the von mises stresses of each of the elements within cluster Ω_i, which themselves each depended upon that element's stress vector, which themselves each depended upon the design variable x_b being differentiated with respect to. This is best expressed by Equation 33, obtained by applying the chain rule. This laid out three separate sensitivities that

would have to be derived. $\frac{\partial \sigma_i^{PN}(x)}{\partial \sigma_a^{VM}}$ would be a scalar, whereas $\frac{\partial \sigma_a^{VM}(x)}{\partial \sigma_a}$ and $\frac{\partial \sigma_a(x)}{\partial x_b}$ were each 6-component vectors since they both included the σ_a stress vector.

$$\frac{\partial \sigma_i^{PN}}{\partial x_b} = \sum_{a \epsilon \Omega_i}^{n_a} \frac{\partial \sigma_i^{PN}(x)}{\partial \sigma_a^{VM}} \left(\frac{\partial \sigma_a^{VM}(x)}{\partial \sigma_a} \right)^T \frac{\partial \sigma_a(x)}{\partial x_b} \tag{33}$$

$\frac{\partial \sigma_i^{PN}(x)}{\partial \sigma_a^{VM}}$ could be derived from the definition of σ_i^{PN} (Equation 16) as follows:

$$\frac{\partial \sigma_i^{PN}(x)}{\partial \sigma_a^{VM}} = \frac{1}{p} \left(\frac{1}{N_i} \sum_{a \epsilon \Omega_i}^{n_a} \left(\sigma_a^{VM}(x) \right)^p \right)^{\frac{1}{p}-1} \cdot \frac{p}{N_i} \left(\sigma_a^{VM}(x) \right)^{p-1}$$

$$\rightarrow \frac{\partial \sigma_i^{PN}(x)}{\partial \sigma_a^{VM}} = \left(\frac{1}{N_i} \sum_{a \epsilon \Omega_i}^{n_a} \left(\sigma_a^{VM}(x) \right)^p \right)^{\frac{1}{p}-1} \cdot \frac{1}{N_i} \left(\sigma_a^{VM}(x) \right)^{p-1} \tag{34}$$

$\frac{\partial \sigma_a^{VM}(x)}{\partial \sigma_a}$ could be derived from the definition of σ_a^{VM} (Equation 17) as follows:

$$\frac{\partial \sigma_a^{VM}(x)}{\partial \sigma_a} = \begin{pmatrix} \dfrac{\partial \sigma_a^{VM}}{\partial \sigma_{ax}} \\ \dfrac{\partial \sigma_a^{VM}}{\partial \sigma_{ay}} \\ \dfrac{\partial \sigma_a^{VM}}{\partial \sigma_{az}} \\ \dfrac{\partial \sigma_a^{VM}}{\partial \sigma_{axy}} \\ \dfrac{\partial \sigma_a^{VM}}{\partial \sigma_{ayz}} \\ \dfrac{\partial \sigma_a^{VM}}{\partial \sigma_{axz}} \end{pmatrix} = \begin{pmatrix} \dfrac{1}{2\sigma_a^{VM}} \left(2\sigma_{ax} - \sigma_{ay} - \sigma_{az} \right) \\ \dfrac{1}{2\sigma_a^{VM}} \left(2\sigma_{ay} - \sigma_{ax} - \sigma_{az} \right) \\ \dfrac{1}{2\sigma_a^{VM}} \left(2\sigma_{az} - \sigma_{ay} - \sigma_{ax} \right) \\ \dfrac{3}{\sigma^{VM}} \sigma_{axy} \\ \dfrac{3}{\sigma^{VM}} \sigma_{ayz} \\ \dfrac{3}{\sigma^{VM}} \sigma_{axz} \end{pmatrix} \tag{35}$$

From Equation 28, the following expression for $\frac{\partial \sigma_a(x)}{\partial x_b}$ was obtained:

$$\frac{\partial \sigma_a(x)}{\partial x_b} = [C^0][B] \left(u_a \frac{\partial E_a}{\partial x_b} + E_a \frac{\partial u_a}{\partial x_b} \right) \tag{36}$$

The u_a element displacement vector was obtained by extracting the global displacement vector entries corresponding to the degree of freedom IDs for that element. The $\frac{\partial E_a}{\partial x_b}$ and $\frac{\partial u_a}{\partial x_b}$ derivatives were derived as in Appendix 8.1. Consequently, the following expression for $\frac{\partial \sigma_i^{PN}}{\partial x_b}$ was obtained.

$$\frac{\partial \sigma_i^{PN}}{\partial x_b} = \sum_{a \epsilon \Omega_i}^{n_a} \left(\frac{1}{N_i} \sum_{a \epsilon \Omega_i}^{n_a} \left(\sigma_a^{VM}(x) \right)^p \right)^{\frac{1}{p}-1} \cdot \frac{1}{N_i} \left(\sigma_a^{VM}(x) \right)^{p-1} \cdot \begin{pmatrix} \frac{1}{2\sigma_a^{VM}} \left(2\sigma_{ax} - \sigma_{ay} - \sigma_{az} \right) \\ \frac{1}{2\sigma_a^{VM}} \left(2\sigma_{ay} - \sigma_{ax} - \sigma_{az} \right) \\ \frac{1}{2\sigma_a^{VM}} \left(2\sigma_{az} - \sigma_{ay} - \sigma_{ax} \right) \\ \frac{3}{\sigma^{VM}} \sigma_{axy} \\ \frac{3}{\sigma^{VM}} \sigma_{ayz} \\ \frac{3}{\sigma^{VM}} \sigma_{axz} \end{pmatrix}^T \cdot [C^0][B] \left(u_a \frac{\partial E}{\partial \rho} \cdot \frac{H(a,b)}{H_s(a)} + E_a \frac{\partial u_a}{\partial x_b} \right) (37)$$

A script was written to assemble a separate global $\frac{\partial \sigma_i^{PN}}{\partial x}$ matrix for each of the i clusters to be used in each of the i optimisations. The number of times Equation 37 had to be computed was therefore equal to the number of elements multiplied by the number of clusters. This imposed a very large computational expense and made the formulation of global $\frac{\partial \sigma_i^{PN}}{\partial x}$ matrices and therefore the stress topology optimisation for the tibial tray unfeasible without extra computational resource. Regardless, the primary focus of the stress topology optimisation work was finding the first five entries of the global $\frac{\partial \sigma_i^{PN}}{\partial x}$ matrices for a simple three-cluster cantilever beam case, before attempting to verify these values by developing a script to calculate finite difference approximations of the values. The finite difference approximation for each global matrix component b of a given cluster i could be found as in Equation 38, and a script was written to implement this. Achieving a verified computation of the P-norm stress sensitivity matrix would essentially constitute the creation of a non-penalising stress topology optimisation, with the only remaining steps being to integrate each cluster's sensitivity matrix into Equation 32 for the respective optimisation and running the simulation on the tibial tray structure using sufficient computational resource.

$$\frac{\partial \sigma_i^{PN}}{\partial x_b} \approx \frac{\sigma_i^{PN}(x_b + \delta x) - \sigma_i^{PN}(x_b)}{\delta x} \tag{38}$$

4. RESULTS

The design results arrived upon following the methodology described were as follows:

1) *'Control'* – All volume fractions made equal to their regional target value to achieve regional modulus targets.

2) *'Stiffness Top Op'* – Stiffness maximising topology optimisation with average regional volume fraction target constraints.

3) *'Stress Limited'* – Volume fractions set such that element yield stresses were made equal to their experienced stresses according to the stress distribution of *'Stiffness Top Op'*.

4) *'Stress Limited Control'* – Volume fractions within the *'Control'* design compared to respective element volume fractions within the *'Stress Limited'* design and adjusted to these values if they are greater.

5) *'Stress Limited Top Op'* – Volume fractions within the *'Stiffness Top Op'* design compared to respective element volume fractions within the *'Stress Limited'* design and adjusted to these values if they are greater.

6) *'Convergent Stress Limited'* – With an initial condition of all elements having volume fractions of 0.08, looping the process of defining a stress limited design based on the stress distribution and making comparisons to form a 'hybrid' design. Looped until convergence with a constraint of no volume fraction exceeding 0.2. Designs 4 and 5 are single iteration cases of this approach with the initial condition being the '*Control'* and *'Stiffness Top Op'* designs respectively.

A solid material design result with all volume fractions set to 1 and a modulus of 110 GPa was also used as a control.

The key result of the non-penalising stress topology optimisation work was comparison of the analytical results obtained with the finite difference P-norm stress sensitivity.

4.1. DESIGN RESULTS

For each design result, the maximum stress, percentage of predicted element failures, average percentage deviation from modulus targets and average volume fractions by region and overall was compared. Additionally, the vertical displacement of the implant at the location described by Figure 27 were compared, as these were expected to be the locations of greatest deflection. The dwell point was the location of load application in the ISO test.
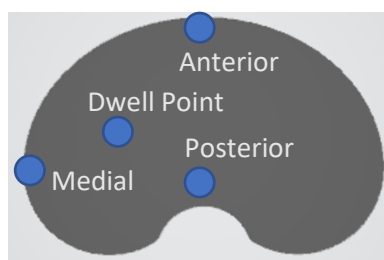

FIGURE 27 – LOCATIONS OF DISPLACEMENT MEASUREMENT

The results were as summarised in Table 4 and Figures 28 and 29. It should be noted that these results were for right-hand side tibial tray designs (the lateral inversion of left-hand side designs).

TABLE 4 – RESULTS FOR THE SIX DESIGNS

	1	2	3	4	5	6	Solid
Maximum Stress (MPa)	22.2	23.1	78.6	63.4	62.4	63.3	22.0
% Predicted Element Failures	40.3%	33.5%	28.2%	22.2%	21.4%	12.0%	0%
% Average Deviation from Modulus Targets	0%	14.3%	22.8%	12.0%	20.8%	95.0%	22674%
Average Volume Fractions							
Overall (Target = 0.080) {% Deviation from Target}	0.08 {0%}	0.08 {0%}	0.079 {1.25%}	0.0895 {11.9%}	0.0863 {7.88%}	0.0981 {22.6%}	1 {1150%}
R1 (Target = 0.080)	0.08	0.08	0.0704	0.0826	0.0818	0.0827	1
R2 (Target = 0.072)	0.072	0.072	0.0928	0.0982	0.093	0.1161	1
R3 (Target = 0.070)	0.07	0.07	0.0896	0.0995	0.0896	0.1389	1
L1 (Target = 0.082)	0.082	0.082	0.0787	0.089	0.0861	0.0945	1
L2 (Target = 0.081)	0.081	0.081	0.0991	0.1074	0.0991	0.1363	1
L3 (Target = 0.079)	0.079	0.079	0.1005	0.1116	0.1005	0.1665	1
Deflection (mm)							
Anterior	0.0334	0.0118	0.00464	0.0189	0.0100	0.0255	0.000175
Posterior	0.0148	0.0092	0.00345	0.00425	0.00380	0.00288	0.0000622
Dwell Point	1.30	0.970	0.596	0.563	0.540	0.441	0.00566
Medial	2.70	2.10	1.20	1.10	1.10	0.782	0.0113

The average percentage deviation from the modulus targets was found from the average absolute percentage deviations from volume fraction targets – equivalent due to the linear relation between the properties. Though similar in formulation, this was non-identical to the percentage deviation from the average overall volume fraction target (Equation 39).

$$\frac{\sum \frac{|Volfracs(:) - Control\,Volfracs(:)|}{Control\,Volfracs(:)}}{No.\,Implant\,Elements} \neq \frac{\frac{\sum Volfracs(:)}{No.\,Implant\,Elements} - \frac{\sum Control\,Volfracs(:)}{No.\,Implant\,Elements}}{\frac{\sum Control\,Volfracs(:)}{No.\,Implant\,Elements}} \tag{39}$$
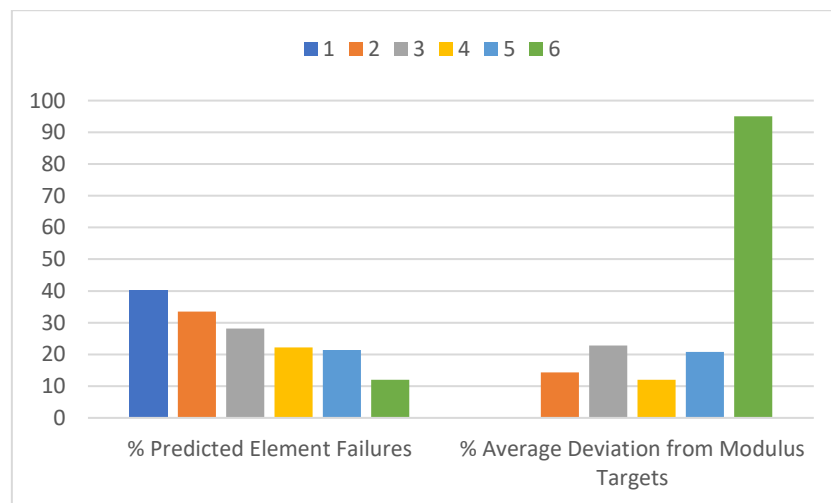

FIGURE 28 – ELEMENT FAILURE AND MODULUS TARGET DEVIATION COMPARISON
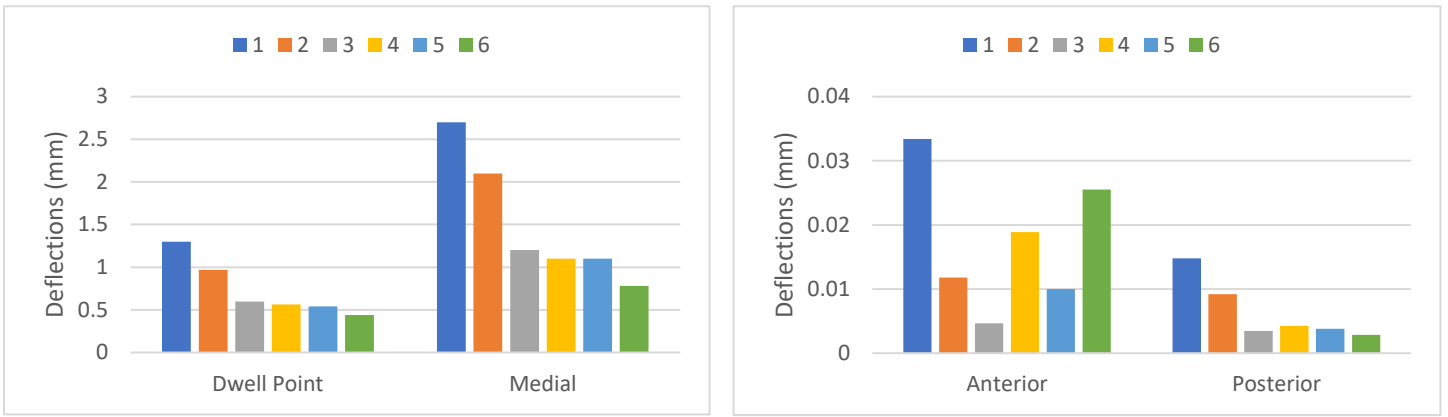
FIGURE 29 – LOCATIONAL DEFLECTION COMPARISON

The volume fraction distribution of each design as well as the stress and element failure distributions are show visually in Figures 30-41.
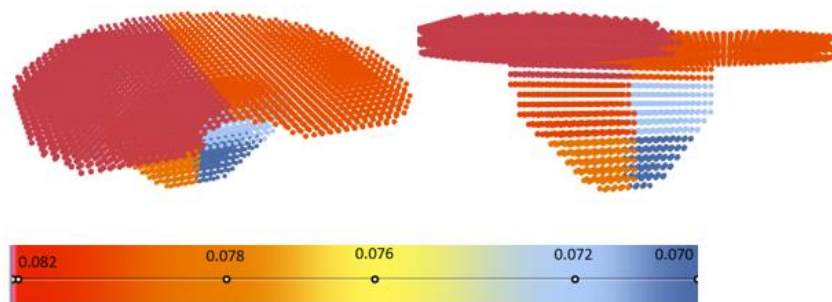
1) 'Control'

FIGURE 30 – 'CONTROL' VOLUME FRACTION DISTRIBUTION VISUALISATION
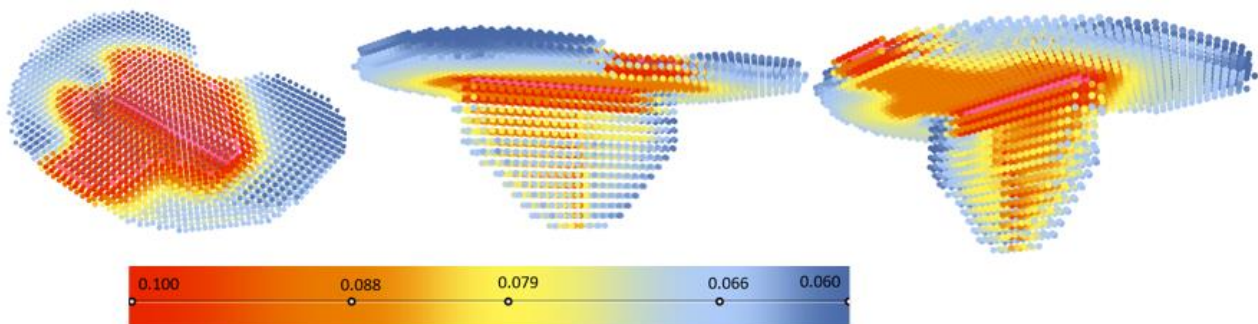
2) 'Stiffness Top Op'

FIGURE 31 – 'STIFFNESS TOP OP' VOLUME FRACTION DISTRIBUTION VISUALISATION
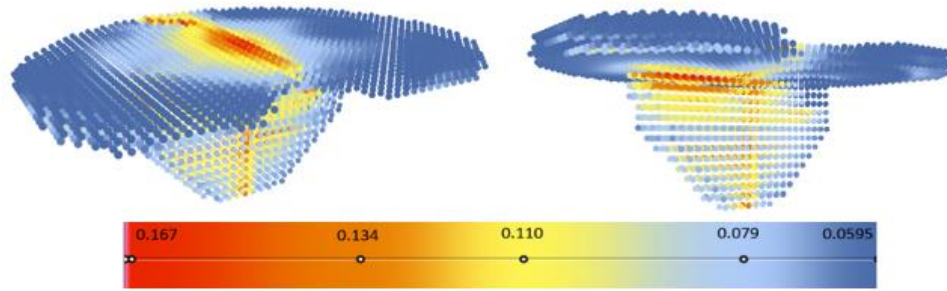
3) *'Stress Limited'*

FIGURE 32 – *'STRESS LIMITED'* VOLUME FRACTION DISTRIBUTION VISUALISATION
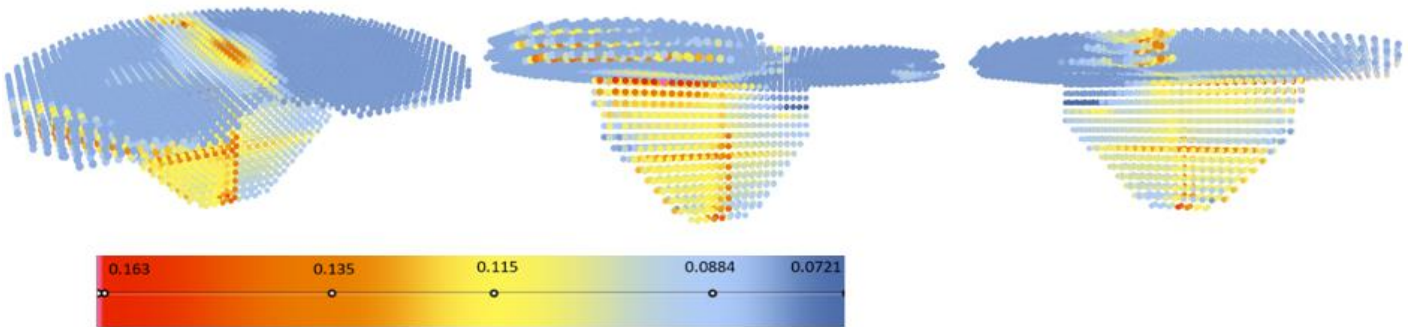
4) *'Stress Limited Control'*

FIGURE 33 – *'STRESS LIMITED CONTROL'* VOLUME FRACTION DISTRIBUTION VISUALISATION
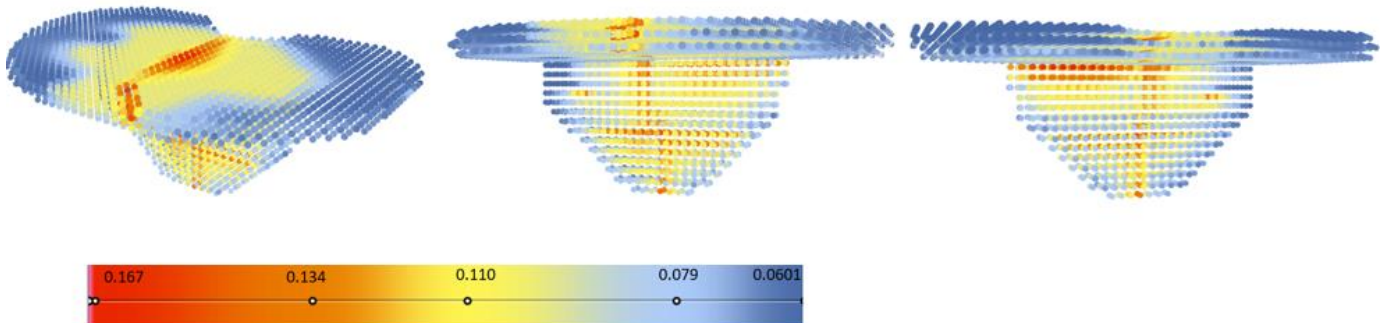
5) *'Stress Limited Top Op'*

FIGURE 34 – *'STRESS LIMITED TOP OP'* VOLUME FRACTION DISTRIBUTION VISUALISATION
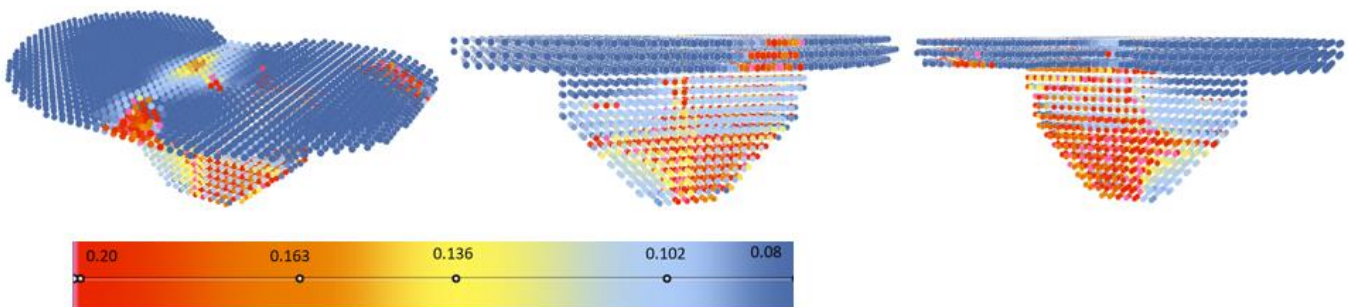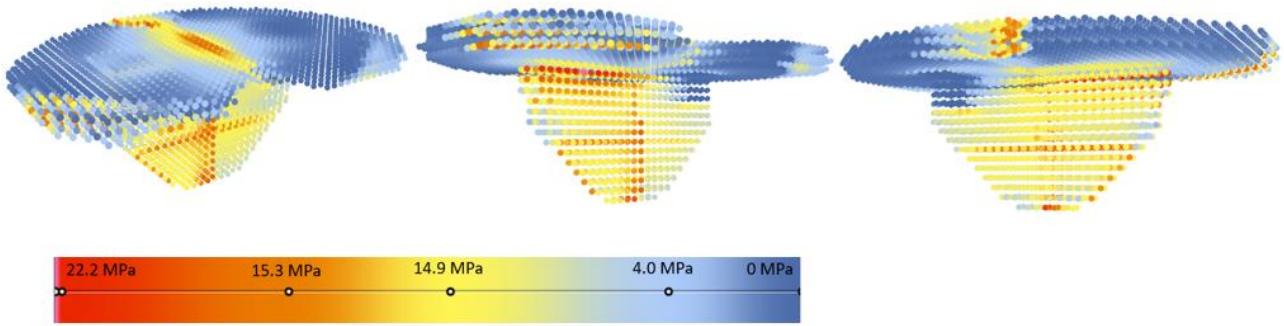
6) *'Convergent Stress Limited'*

FIGURE 35 – *'CONVERGENT STRESS LIMITED'* VOLUME FRACTION DISTRIBUTION VISUALISATION

1) *'Control'*

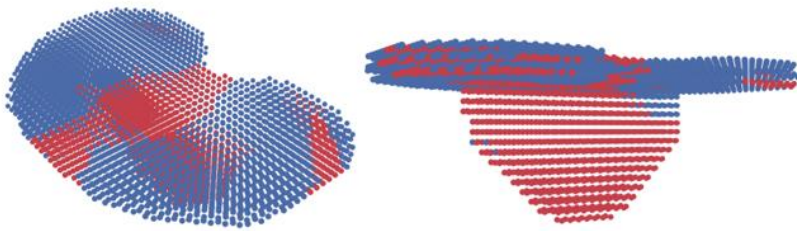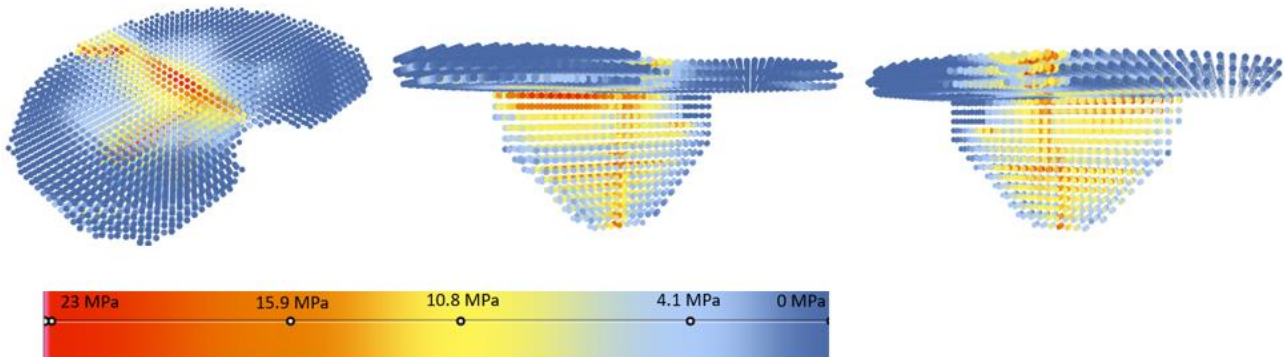**Stresses**

Failures

FIGURE 36 – *'CONTROL'* STRESS AND FAILURE DISTRIBUTION VISUALISATION

2) *'Stiffness Top Op'*
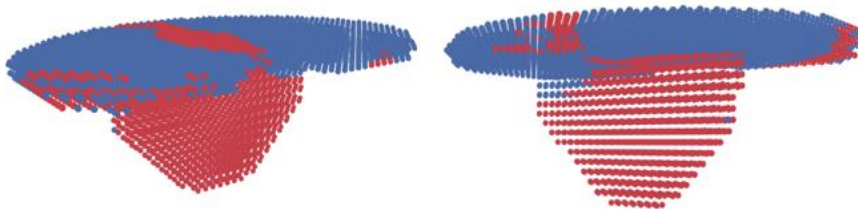
Stresses

Failures

FIGURE 37 – *'STIFFNESS TOP OP'* STRESS AND FAILURE DISTRIBUTION VISUALISATION

3) *'Stress Limited'*

Stresses
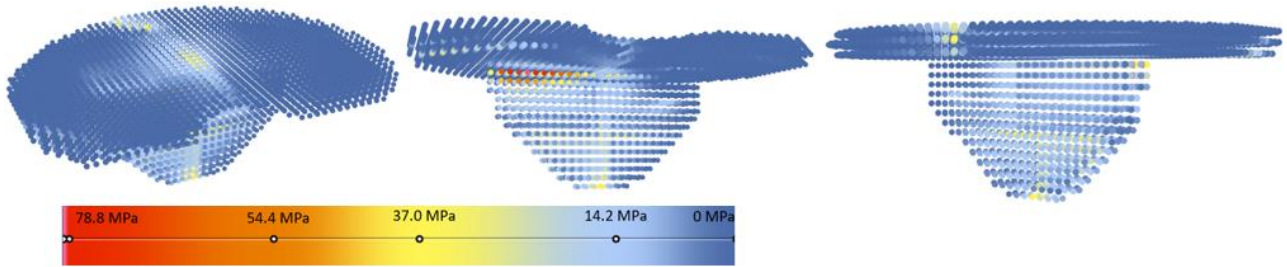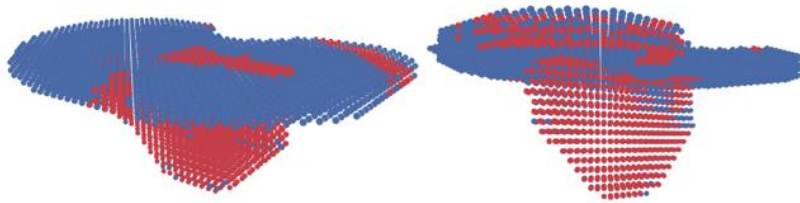
Failures

FIGURE 38 – *'STRESS LIMITED'* STRESS AND FAILURE DISTRIBUTION VISUALISATION

4) *'Stress Limited Control'*

Stresses
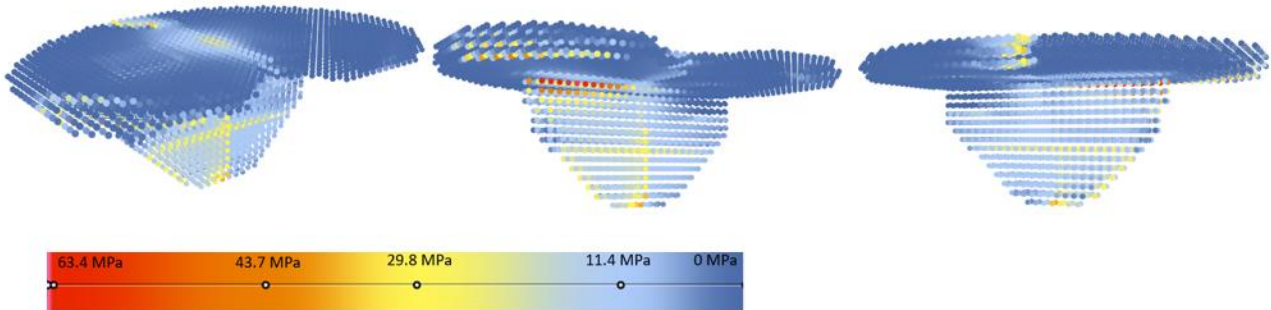
Failures
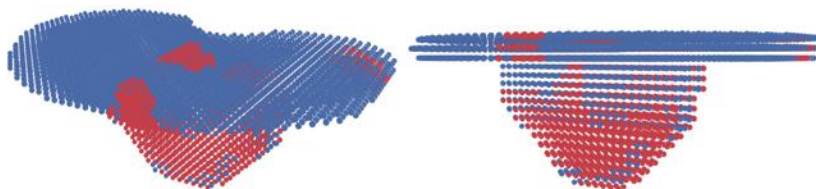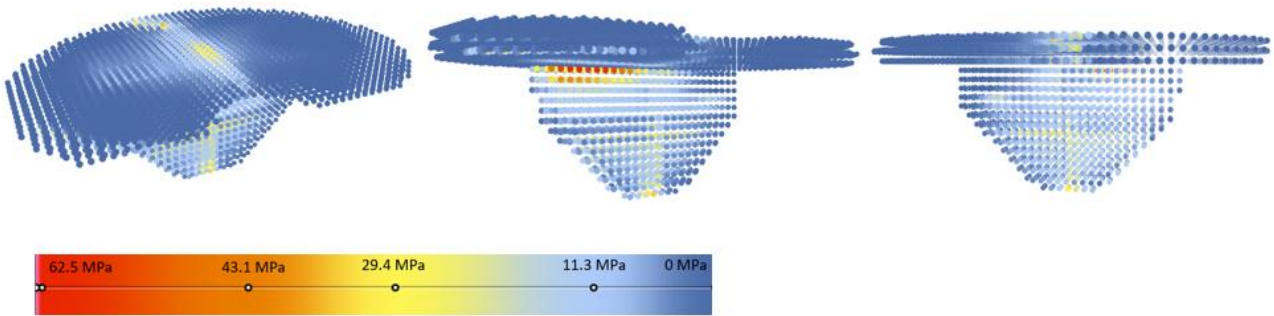

FIGURE 39 – *'STRESS LIMITED CONTROL'* STRESS AND FAILURE DISTRIBUTION VISUALISATION

5) *'Stress Limited Top Op'*
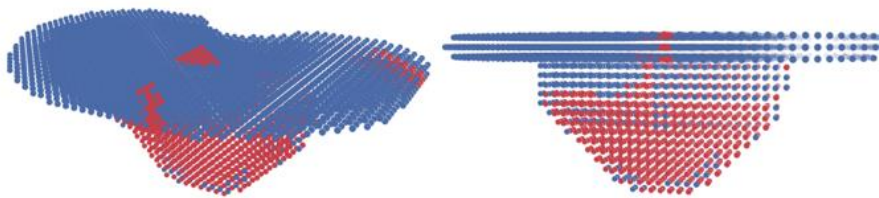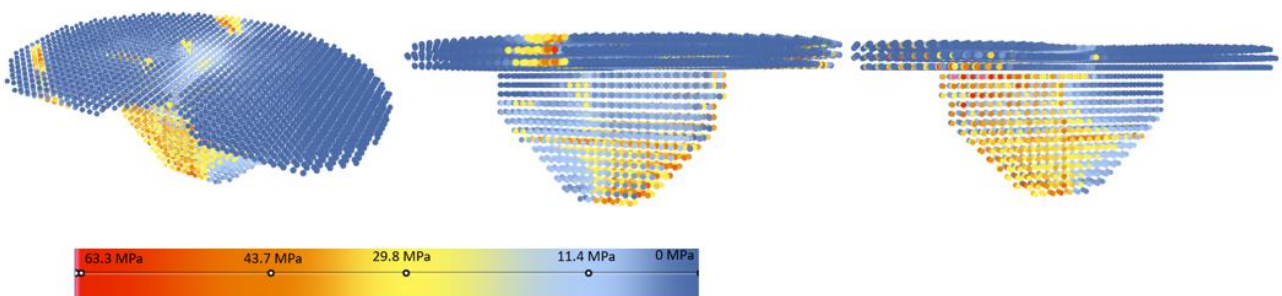
Stresses

Failures

FIGURE 40 – *'STRESS LIMITED TOP OP'* STRESS AND FAILURE DISTRIBUTION VISUALISATION

6) *'Convergent Stress Limited'*
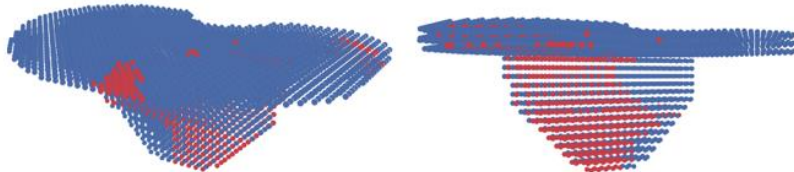
Stresses

Failures

FIGURE 41 – *'CONVERGENT STRESS LIMITED'* STRESS AND FAILURE DISTRIBUTION VISUALISATION

4.2. P-NORM STRESS SENSITVITY RESULTS

Table 5 shows the P-norm stress sensitivity values with respect to the first 5 elements for each of three clusters in a cantilever beam with a 900 N end point loading, calculated by the analytical solution derived in Section 3.6.2. These were compared with finite difference approximations for these values, using a δ of 0.01 (Table 6) and δ of 0.05 (Table 7).

TABLE 5 – ANALYTICAL P-NORM SENSITIVITY VALUES

	w.r.t element 1	w.r.t. element 2	w.r.t element 3	w.r.t element 4	w.r.t element 5
Cluster 1	-8.4E+09	-8.9E+09	-1.3E+10	-1.4E+10	-1.6E+10
Cluster 2	-5.5E+07	-5.6E+07	-4.6E+07	-4.9E+07	-3.2E+07
Cluster 3	-7E+07	-7.5E+07	-5.5E+07	-1.1E+08	-3.8E+07

TABLE 6 – FINITE DIFFERENCE P-NORM SENSITIVITY VALUES WITH $\delta = 0.01$

	w.r.t element 1	w.r.t. element 2	w.r.t element 3	w.r.t element 4	w.r.t element 5
Cluster 1	-1.10E+07	-1.10E+07	-6860722	-6860722	-2645628
Cluster 2	-277265	-277265	-202156	-202156	-237028
Cluster 3	-97015.3	-97015.3	-85985.2	-85985.2	-247305

TABLE 7 – FINITE DIFFERENCE P-NORM SENSITIVITY VALUES WITH $\delta = 0.05$

	w.r.t element 1	w.r.t. element 2	w.r.t element 3	w.r.t element 4	w.r.t element 5
Cluster 1	-1.10E+07	-1.10E+07	-6795869	-6795869	-2612158
Cluster 2	-265780	-265780	-196178	-196178	-231058
Cluster 3	-74089.4	-74089.4	-78222.2	-78222.2	-240199

5. DISCUSSION

5.1. KEY FINDINGS

The most important findings of the project were as summarised:

- The non-penalising stiffness-maximising topology optimisation offers a 16.9% improvement of failure behaviour compared to the *'Control'* design, with 33.5% of tibial tray elements predicted to fail in the former compared with 40.3% in the latter. This was achieved with a relatively low average deviation from element modulus targets of 14.3%.

- The *'Stress Limited'* and hybrid solutions all reduced the predicted element failure percentage further. Though the *'Stress Limited'*, *'Stress Limited Top Op'* and *'Convergent Stress Limited'* designs do so with a compromise of greater average deviation from

modulus targets compared to the *'Stiffness Top Op'* design, the *'Stress Limited Control'* design in fact reduces the average deviation from modulus targets to 12.0%, as well as reducing the predicted element failures to 22.2% (a 44.9% improvement upon the *'Control'*).

- In light of this, a convergent solution was sought with the initial condition set to the *'Control'* design. This resulted in predicted element failures going down to 11.4% with a 23.4% average modulus target deviation. This represents a significant improvement upon the *'Convergent Stress Limited'* design, where 12.0% of elements were predicted to fail with a 95.0% average modulus target deviation. This demonstrates the strong initial condition sensitivity of the convergent stress limiting approach – using the actual targets in the initial condition design instead of a design with a continuous volume fraction equal to the average overall target value of 0.08 gave a similar percentage element failure prediction but with much better modulus matching. The process' initial condition design and iteration number could therefore be tuned to arrive upon the desired compromise between failure behaviour and bone remodelling.

- A minimum continuous volume fraction of 0.17 was needed for no element failures to be predicted. The average deviation from the target moduli in this case was 112.5%.

- Failure behaviour, modulus target deviation and all deflections except at the anterior point had similar general trends between designs – decreasing failure and displacement but increasing modulus target compromise in the following: order *'Control'*, *'Stiffness Top Op'*, *'Stress Limited'* and single-iteration hybrid results, *'Convergent Stress Limited'*, fully solid. The trend in anterior point deflections between designs was less predictable.

- For P-norm sensitivities, analytical results were consistently an order of 2-3 greater than the finite difference approach. The analytical solution derivation and implementation should be further investigated, particularly the $\frac{\partial K}{\partial x_b}$ matrix formulation, which is suspected to be the source of error for its complexity.

5.2.   COMPARISONS TO LITERATURE

Peto et al. investigated a SIMP binary compliance-minimising topology optimisation with a weight constraint, performed upon the mid region of the head of an intramedullary knee implant [28]. This was found to increase the magnitude of the maximum deflection and von mises stress by 14.4% and 1.7% respectively, when a 30% weight reduction constraint was set. Since solid stainless steel material was used, the yield stress was constant and far greater than the maximum

stress before and after the optimisation, and failure behaviour therefore did not need to be considered. The non-penalising compliance-minimising topology optimisation in this project also increased the maximum von mises stress marginally, by 4.1%, but the maximum measured deflection fell by 22.2%. The typical SIMP approach minimises compliance subject to a minimum void-creation constraint, whereas the non-penalising approach developed in this project minimised compliance with a constraint on the maximum average volume fraction, without seeking to create any voids. This may explain why the maximum deflection values change in opposite directions in the two cases – for the former approach, though element stiffness values are maximised, the void creation results in a stiffness reduction of the overall structure.

Boccini et al. conducted a lattice-integrating SIMP compliance-minimising topology optimisation upon a turbine disc using the OptiStruct solver, with constraints upon the vibration mode, maximum stress, and volume reduction [29]. A relaxed penalisation factor of 1.8 was used to achieve a design containing intermediate design variable values, before assigning element with high values as solid material, those with low values as voids and those with intermediate values as lattice material with strut radii proportional to the intermediate value of that element. The solution saw a 17% reduction in mass and 6% reduction in maximum stress compared to the original design. The favourable outcome is encouraging for the mass-minimising, stress-constrained topology optimisation considered in Section 3.6. Expected outcomes may be investigated by running an OptiStruct optimisation on the tibial tray with such an objective function and constraint, using a penalisation factor of 1 and defining an appropriate range on intermediate-classified design values to achieve a fully lattice structure design. A deficiency in the OptiStruct solver is a lack of volume fraction-yield strength relation implementation, necessitating an overly conservative stress constraint as discussed in Section 3.6.

5.3. LIMITATIONS

One major limitation of the results obtained as evidenced by the stress distributions for all designs was the insufficient element thickness of the plateau region. The region was three elements thick, but due to the loading condition, would experience a bending stress. The σ_{xx} in the plateau region would therefore vary drastically through the thickness, from a maximum positive tensile stress at the top to an equal magnitude negative compressive stress at the underside. The very low stress values of all design's off-centre plateau regions suggest that the stresses evaluated at element centroids here were too close to the neutral axis, failing to capture the large through-thickness

change. The designs therefore underpredicted stresses in this region. Two possible mitigations could be implemented in future work. Firstly, a finer mesh could be used overall or in the plateau region. However, this would have increased the computational expense significantly. Alternatively, while the stress vectors had been evaluated at element centroids in this project, the true potential stresses experienced by each element could have been captured by evaluating stress vectors at each node and Gauss point as in Section 3.4.2, finding von mises stresses from each, and assigning the element's von mises stress as the greatest of these. This would increase the stress evaluation function's run time by a factor of eight.

Another limitation of the project was the data available from which to draw the modulus-volume fraction relation of Figure 9 and the yield stress-volume fraction relation of Figure 23. The trendlines were drawn from only five datapoints, with the lowest volume fraction datapoint being 0.076, therefore requiring the trend to be extrapolated throughout the simulations. An improved trendline could be drawn by conducting material testing on a greater number of lattice material specimens concentrated in the volume fraction range of 0.05-0.2.

Applying the continuum assumption inherent in the finite element methods to the lattice structure may be another limitation. A more accurate but infeasible approach would be to model a solid continuum at the location of the struts only, to perfectly map the lattice architecture, and account for the complex, micro-level strut stress behaviour as described in Section 2.3. Nevertheless, literature suggests that a continuum assumption is valid for a lattice structure provided the response is not dominated by in-plane motion of single-layer grids [30], which the lattice structured tibial tray is expected to satisfy.

5.4.   CLINICAL SIGNIFICANCE

The potential to improve bone remodelling behaviour by matching the modulus values of a knee implant's tibial tray with its surrounding tibia material has been well understood by the Biomechanics Group. However, without ISO certification, the implant design cannot be approved for use in knee arthroplasty patients, due to fatigue failure risks. Failure behaviour-improving methodologies, designed to retain remodelling capability to a reasonable degree, have been presented, which may be developed further to achieve an ISO-certified design.

6. CONCLUSIONS

This project develops three key potential avenues to adjusting an additive manufactured lattice structure tibial tray design with ideal load-translating behaviour. The effective translation of loads from the tibial tray to the surrounding tibia, achieved by matching the component's anisotropic moduli to that of the surrounding bone, negates the typical stress-shielding effect which results in bone weakening and potential complication following arthroplasty in modern knee implants. The adjustments seek to improve the yield behaviour of the design, with a view to improve ISO test performance, with a compromise of greater deviation from imposed modulus targets. The non-penalising stiffness-maximising topology optimisation approach improved yielding behaviour by 16.9%. The stress limiting approach developed, which attempted to iteratively match the yield stress through the structure with the stress experienced, offered further improvement in the yielding behaviour. The degree of compromise upon modulus targets proved highly sensitive to initial condition designs and iteration number, offering scope for further exploration. The *'Stress Limited Control'* design resulted from a single iteration upon a fully modulus-matched design and improved failure behaviour by 44.9% with only a 12.0% average deviation from modulus targets. A novel non-penalising stress-constrained topology optimisation would be the most holistic and efficient way to adjust the tibial tray design, the groundwork for which has been investigated.

7. REFERENCES

[1] Zehtab M et al., Current Trends in Knee Arthroplasty. Global Journal of Health Science 2016 July 25,;9:234.

[2] Culliford D et al., Future projections of total hip and knee arthroplasty in the UK: results from the UK Clinical Practice Research Datalink. Osteoarthritis and cartilage 2015;23(4):594-600.

[3] Total Knee Replacement - OrthoInfo - AAOS. Available at: https://www.orthoinfo.org/en/treatment/total-knee-replacement/

[4] Lewis PL et al., Variation and trends in reasons for knee replacement revision: a multi-registry study of revision burden. Acta Orthopaedica 2020 December 2,;0(0):1-7.

[5] O'Brien S et al., Prediction of backside micromotion in total knee replacements by finite element simulation. Proceedings of the Institution of Mechanical Engineers. Part H, Journal of engineering in medicine 2012 March 1,;226:235-45.

[6] Munford M, Hossain U, Ghouse S, Jeffers J. Prediction of Anisotropic Mechanical Properties for Lattice Structures. Additive Manufacturing 2020 March 1,;32:101041.

[7] Munford MJ, Ng KCG, Jeffers JRT. Mapping the Multi-Directional Mechanical Properties of Bone in the Proximal Tibia. Advanced Functional Materials 2020;30(46):2004323.

[8] Kutzner I et al., Loading of the knee joint during activities of daily living measured in vivo in five subjects. J Biomech 2010 -08-10;43(11):2164-73.

[9] Au AG et al., Contribution of loading conditions and material properties to stress shielding near the tibial component of total knee replacements. J Biomech 2007;40(6):1410-6.

[10] Teichtahl A et al., Wolff's law in action: A mechanism for early knee osteoarthritis. Arthritis research & therapy 2015 September 1,;17:207.

[11] Tyrovola J. The "mechanostat theory" of frost and the OPG/Rankl/RANK system. Journal of cellular biochemistry 2015 June 20,;116.

[12] Gobbo L et al., Are Associated with Bone Mineral Density and Physical Function in Older Adults: Cross-Sectional and Prospective Data. International Journal of Environmental Research and Public Health 2020 November 6,;17.

[13] Bahraminasab M et al., Aseptic loosening of femoral components - Materials engineering and design considerations. Materials and Design 2013 February 1,;44:155-63.

[14] Chen Z et al., Biomechanics and Tribology of Artificial Knee Joint. ; 2019, p. 191-239.

[15] Maietta S et al., A Further Analysis on Ti6Al4V Lattice Structures Manufactured by Selective Laser Melting. 2019; Available at: https://www.hindawi.com/journals/jhe/2019/3212594/.

[16] ISO 14879-1:2020. Available at: https://www.iso.org/cms/render/live/en/sites/isoorg/contents/data/standard/07/23/72356.html.

[17] Seharing A, Azman AH, Abdullah S. A review on integration of lightweight gradient lattice structures in additive manufacturing parts. Advances in Mechanical Engineering 2020 June 1,;12:168781402091695.

[18] Maconachie T et al., SLM lattice structures: Properties, performance, applications and challenges. Materials & design 2019 Dec 5,;183:108137.

[19] Zargarian A et al., Theoretical and applied fracture mechanics. 2019 April 1,;100:225-32.

[20] Mazur M et al., Deformation and failure behaviour of Ti-6Al-4V lattice structures manufactured by selective laser melting (SLM). 2015.

[21] Zhu J et al., A review of topology optimization for additive manufacturing: Status and challenges. Chinese journal of aeronautics 2021 Jan;34(1):91-110.

[22] Erik Holmberg. Stress and fatigue constrained topology optimization; 2013.

[23] Biyikli E, et al., Proportional Topology Optimization: A New Non-Sensitivity Method for Solving Stress Constrained and Minimum Compliance Problems and Its Implementation in MATLAB. PLOS ONE 2015 17-Dec-;10(12):e0145041.

[24] Gebremedhen HS, Woldemicahel DE, Hashim FM. Three-dimensional stress-based topology optimization using SIMP method. Int. J. Simul. Multidisci. Des. Optim. 2019;10:A1.

[25] De Leon D, Fagundes Gonçalves J, de Souza C. Stress-based topology optimization of compliant mechanisms design using geometrical and material nonlinearities. Structural and Multidisciplinary Optimization 2020 July 1,.

[26] Liu K, Tovar A. An efficient 3D topology optimization code written in Matlab. Structural and Multidisciplinary Optimization 2014 December 1,;50.

[27] Papadimitriou DI, Giannakoglou KC. Aerodynamic shape optimization using first and second order adjoint and direct approaches. Archives of Computational Methods in Engineering 2008;15(4):447-88.

[28] Peto M et al., Structural design optimization of knee replacement implants for Additive Manufacturing. Procedia Manufacturing 2019 January 1,;34:574-83.

[29] Boccini E et al., Toward the integration of lattice structure-based topology optimization and additive manufacturing for the design of turbomachinery components. Advances in Mechanical Engineering 2019;11(8):1687814019859789.

[30] Noor A, Martin M. Continuum Modeling of Large Lattice Structures: Status and Projections. 1988 March 1,.

8. APPENDIX

8.1. DERIVATIONS

8.1.1. $\frac{\partial E_a}{\partial x_b}$ DERIVATION

The modulus of an element depends upon the volume fraction of that element ρ_a only, which leads to the expression for $\frac{\partial E_a}{\partial x_b}$ below, by applying chain rule.

$$\frac{\partial E_a}{\partial x_b} = \frac{\partial E_a}{\partial \rho_a}\frac{\partial \rho_a}{\partial x_b}$$

Since a linear relation between moduli and volume fractions was fitted, $\frac{\partial E_a}{\partial \rho_a}$ was trivial and identical for all elements. The filtering scheme implementation adopted from *top3d* calculated a vector of all ρ values from a vector of all design variables using the [number of elements x number of elements] sized matrix H and the [number of elements x 1] sized vector Hs as below.

$$\rho(:) = (H \times x(:)) \cdot / H_s$$

The $\frac{\partial \rho_a}{\partial x_b}$ value, representing the element b weight factor contribution to ρ_a, could therefore be extracted as follows:

50

$$\frac{\partial \rho_a}{\partial x_b} = \frac{H(a,b)}{H_s(a)}$$

8.1.2. $\frac{\partial u_a}{\partial x_b}$ DERIVATION

The derivation process was to first find $\frac{\partial U}{\partial x_b}$ before extracting those entries corresponding to the degree

of freedom IDs of element a to find $\frac{\partial u_a}{\partial x_b}$. Differentiating through the global force-displacement

relation and applying the product rule gave $\frac{\partial U}{\partial x_b}$ as follows:

$$[K][U] = [F]$$

$$\frac{\partial K}{\partial x_b}[U] + \frac{\partial U}{\partial x_b}[K] = 0$$

$$\frac{\partial U}{\partial x_b} = -[K]^{-1}\frac{\partial K}{\partial x_b}[U]$$

Since the $[K]$ matrix depends upon the modulus values of all elements, which itself depends on

the respective element volume fraction, $\frac{\partial K}{\partial x_b}$ was a matrix of equal size to the stiffness matrix,

assembled as follows by the chain rule:

$$\frac{\partial K}{\partial x_b} = \sum_{e=1}^{n_e} \frac{\partial K}{\partial E_e}\frac{\partial E_e}{\partial \rho_e}\frac{\partial \rho_e}{\partial x_b}$$

$\frac{\partial E_e}{\partial \rho_e}$ was a constant found from the linear relation between modulus and volume fraction. $\frac{\partial \rho_e}{\partial x_b}$ was

the element b weight factor contribution to ρ_a, equal to $\frac{H(e,b)}{H_s(e)}$. The $\frac{\partial K}{\partial E_e}$ matrix was of equal size to

the stiffness matrix, with all entries zeroed apart from the 24 x 24 entries corresponding to the

degree of freedom IDs of element e. These were set equal to the corresponding K matrix entries

divided by E_e. $\frac{\partial U}{\partial x_b}$ was thus found, from which $\frac{\partial u_a}{\partial x_b}$ could be extracted as follows:

$$\frac{\partial U}{\partial x_b} = -[K]^{-1}\left(\frac{\partial E}{\partial \rho}\sum_{e=1}^{n_e}\frac{\partial K}{\partial E_e}\frac{H(e,b)}{H_s(e)}\right)[U]$$

$$\frac{\partial u_a}{\partial x_b} = \frac{\partial U}{\partial x_b}(DOF\ IDs\ of\ a)$$